2023

Quantifying Glial-Glial Interactions In Drosophila Using Automated Image Analysis

Gabriela Salazar Lopez
University of Vermont

QUANTIFYING GLIAL-GLIAL INTERACTIONS IN *DROSOPHILA* USING AUTOMATED IMAGE
ANALYSIS

A Thesis Presented

by

Gabriela Salazar Lopez

To

The Faculty of the Graduate College

Of

The University of Vermont

In Partial Fulfilment of the Requirements
For the Degree of Master of Science
Specializing in Complex Systems and Data Science

August, 2023

Defense Date: August 3rd, 2023
Thesis Examination Committee:

Chris Danforth, Ph.D., Advisor
Melissa Pespeni, Ph.D., Chairperson
John Mathew Mahoney, Ph.D.
Cynthia J. Forehand, Ph.D., Dean of the Graduate College

Abstract

Imaging is an immensely powerful tool in biomedical research. Technological advances in the last half century have led to the development of new tools for image analysis, with major strides being made in the last 20 years especially with machine and deep learning. However, researchers still often hit a bottleneck during the image analysis phase of their projects that often leads to delays and sometimes even limits the scope of their studies. In this thesis I demonstrate some of the issues that arise while quantifying images to answer a biological question by using a dataset of fly central nervous system images to elucidate interactions between different cells. I present an overview of the types of methods that can be used to perform this analysis including a discussion of their advantages and disadvantages. Finally, I present steps for creating and validating an automated image analysis pipeline that was used to analyze a large section of the fly ventral nerve cord, akin to the spinal cord. Automating image quantifying allowed us to maximize the size of the dataset analyzed, which revealed subtle patterns in cell-cell interactions that would not have been uncovered with manual quantification of a smaller dataset.

Citation

Material from this thesis has been published in the following form:

Salazar G., Ross, G., Maserejian, A.E., and Coutinho-Budd, J.. (2022) Quantifying Glial-Glial Tiling Using Automated Image Analysis in Drosophila. Front. Cell. Neurosci. 16:826483. doi: 10.3389/fncel.2022.826483

Material from this thesis was part of an unpublished individual class project paper:

Salazar G.. (2020) Classification of Fly Brain Images. Data Science II, University of Vermont, Individual class project paper.

Acknowledgements

To my "beautiful fat girl" Heidi - a lovely boxer full of energy, joy, and love that provided a tremendous amount of emotional support over the last eight years, and peacefully passed in early 2023.

To my parents and sister - Estela, Rafael, and Lili - who have been there for me for the last 30+ years.

To my beautiful baby niece Georgia, who is so smart, strong, energetic, and continues to be a pleasure to watch grow up.

To Jacob for letting me hang out at his apartment while writing most of this thesis, and to close friends that have gotten me through the last, very stressful, few years.

To all lab and classmates that have worked on this project. Special thanks to the directors of the Deep Learning for Microscope Images course at the Marine Biology Labs. Their knowledge of image analysis, creativity and generosity is truly inspiring. And most thanks to Jaeda, my advisor, a glia expert who gave me the freedom to really take a deep dive in something "totally outside her wheelhouse".

Table of Contents

List of Figures

Chapter 1: Using images to study glial-glial interactions

1.1 Introduction

Humans are visual creatures. When we want to study something, one of our first instincts is to look at it. Researchers and medical doctors have been dissecting animals and human cadavers for hundreds of years in an attempt to understand the inner workings of the human body. The invention of the compound microscope in the mid seventeenth century allowed scientists to magnify tissues and living organisms, eventually leading to the revolutionary discovery that large organisms are made of smaller units, called cells, a term coined by Hooke when he magnified a piece of cork in the 1660s [1]. The discovery of cells is an early example of the crucial role which imaging technology has played in biological research. We have made great strides towards visualizing what we cannot see with the naked eye: from magnifying very tiny objects, for example imaging subcellular components by using electron microscopes, which use electron beams instead of light [2]; distinguishing between items we cannot typically distinguish, e.g. color-coding proteins with fluorescent immunohistochemistry, where proteins are tagged with different colored fluorophores which emit different colors of light when excited by specific wavelengths [3], [4]; and even using non-invasive imaging to visualize the inside of a living organisms, for instance computed tomography (CT) [5] and ultrasounds [6]. Furthermore, we often combine different elements: for example magnification, tagging, and non-invasive imaging in technologies such as functional magnetic resonance imaging (fMRI), which uses blood flow as a proxy to detect activated brain areas in living patients [7]. These incredible technologies allow us to collect images and videos containing extensive information, even a single patient brain scan contains a wealth of data. Unfortunately analyzing these visual datasets has become a bottleneck that significantly slows the progress of many research projects. Though there are various software packages for analyzing biomedical images, they often suffer from issues such as a lack of generalizability to various applications, a steep learning curve, and a prohibitive financial cost in the case of closed-source software. Hence, many labs resort to manual quantification, which comes with its own sets of challenges: being very time consuming is often the main issues, however, a high level of area expertise is required for analyzing specific types of images, and bias may be a major concern in the case of qualitative analyses.

The focus of this thesis is how to address some of the main challenges faced by biomedical researchers during the image analysis phase of their studies. I analyzed a dataset of fruit fly brain images to explore the interactions between different brain cell subtypes. However, many of the same issues arise when analyzing other types of biomedical images. First, I discuss the quantification that was the goal of this project, and how it would allow for the interrogation of cell-cell interactions. Second, I discuss the different steps that were necessary for this quantification and different approaches that can be used to accomplish them. Next, I present a published article that includes the final image analysis pipeline, along with its results. Finally, I discuss some of the pitfalls of the pipeline, and ways in which it can be improved.

1.2 *Drosophila melanogaster* as a model for glial-glial interactions

The human central nervous system (CNS) is the epitome of a complex system. It can be subdivided at many different scales: containing just two parts at the largest scale, the brain and spinal cord, and billions, perhaps trillions, of parts when considering all the pieces present at the subcellular scale: organelles, proteins, DNA and RNA molecules, etc. At the cellular level, it is estimated the CNS contains billions of individual cells [8], each of which interacts with others creating a vast and dynamic network of interactions between these billions of units [9]–[13]. The cells of the CNS can be broadly categorized into two large groups: neurons and glia, which can be further subdivided into dozens of neuronal [14]–[16] and glial subtypes [17]–[19]. Historically, neurons, which form intricate webs through which they send electrochemical messages [9], have received most of the attention from neuroscience researchers, while glia were thought to simply provide a supporting role [20]. However, mounting evidence has shown how essential glia are to proper brain function: from their extensive interactions with neurons [21]–[23], their key roles in development [24]–[27] and injury [28]–[31], and the fact that there is a glial abnormality or deficiency contributing to a great number of neurodevelopmental [24], [26], [32], [33], neurodegenerative [34]–[36], and even psychiatric conditions [24], [37]–[39]. Hence, the field has shifted to include glia in their focus of research. From the perspective of interactions, the field has long focused on neuron-neuron interactions, and there is now much attention on neuron-glia interactions[40]. However, though there is compelling evidence of glial-glial interactions [41], strongly suggested by the repeated observation of glial

2

tiling [42]–[48], there is still little known about the mechanisms underlying these types of interactions. Tiling refers to how glia will cover large areas with minimal overlap into each other's territory (Fig. 2.1 B-G), a phenomenon that is conserved among many species: from flies to humans. We hypothesize glia would have to communicate with one another to establish their territories. Communication would be especially necessary in the case of cells with a branching morphology, or shape, such as astrocytes (Fig. 2.1F), where the mass of cell does not fully occupy its entire territory, and physics is not enough to explain why two cells do not occupy the same region. Hence, studying the underlying mechanism for glial tiling can be used to explain a phenomenon that is presumably important to brain function, evidenced by its high level of conservation, as well as elucidate glial-glial interactions, an understudied area of neuroscience but likely also crucial to proper CNS function given the importance of glia to the overall system.

As discussed previously, the human CNS is incredibly complicated, that along with ethical and practical concerns regarding human experimentation, means the neuroscience community often turns to animal models to elucidate how the system functions. With its great balance between complexity and simplicity, *Drosophila melanogaster,* the fruit fly, provides a particularly useful model for the human CNS. Like its mammalian counterpart, the fly CNS is composed of an abundance of subunits that interact in such a way as to allow for the organism to accomplish a variety tasks: from sensing its environment [49], [50], moving [51], and even interacting socially with other organisms through actions such as aggressive fighting [52] and courtship dances [53]. Furthermore, at the cellular level the fly also consists of several subtypes of neurons [54], [55] and glia [56]. Finally, key to biomedical research: there is a large degree of conservation of genes, proteins, pathways, and CNS substructures from the fly to humans, such that what we learn in the fly remains relevant and useful to human medicine [57].

Nonetheless, the fly CNS is much simpler than the human, and even the mouse CNS, another common animal model used in biomedical research. First, the simplicity of fly genetics has allowed for the development of a whole arsenal of tools that can manipulate individual cell types with exquisite spatiotemporal precision (Fig. 2.1G)[58]. Furthermore, the compartmentalization of the fly CNS is extremely convenient for researchers to investigate interactions between different cell types. In the mammalian CNS, the three main glial subtypes are astrocytes, oligodendrocytes and microglia. Astrocytes

interact with synapses, provide neurons with metabolic support, interact with synapses, and guide neuronal axons, the part of the neuron that carries the signal to the next neuron, to connect with the appropriate partner. Oligodendrocytes wrap axons to increase the speed of signaling and microglia engulf debris in the CNS [20]. In mammals, the different glial subtypes are intermixed with the neuronal somas, or cell bodies, as well as the synapses. The lack of spatial segregation, along with a smaller number of genetic tools for mammalian models, makes it difficult to determine specifically which cells are interacting. In the fly, neuronal cell bodies are located in the cortex, while synapses are located in the neuropil (Fig. 2.1A-A') [56]. Additionally, each glial subtype is located only in a specific location in the CNS. Perineurial and subperineurial glia envelop the CNS to form the blood-brain barrier. Cortex glia, located in the cortex, surround the somas, provide trophic support and engulf debris in the cortex. Astrocytes and ensheathing glia are located in the neuropile. Astrocytes interact with synapses and engulf debris during development. Ensheathing glia form a barrier between the cortex and neuropile and engulf synaptic fragments after injury (Fig. 2.1A-A')[56]. In addition to compartmentalization, flies exhibit tiling not only between glia of the same subtype, but also between glia of different kinds [Fig. 2.1G]. It is this interclass tiling phenomenon that we have exploited to interrogate glial-glial interactions.

Previous work has shown that a cortex-glia specific manipulation, a knockdown or reduction in the amount of the aSNAP or Spz3 proteins, produces a stark morphological change from reticular to globular cells (Fig. 2.1I-I', J-J'). Additionally, there is a breakdown in the spatial segregation normally exhibited by fly glia [40]. In control animals, the cortex contains cortex glia as the single glial subtype in this region (Fig. 2.1H, I-I"). However, in the presence of globular cortex glia, animals exhibit aberrant infiltration into the cortex by astrocytes (Fig. 2.1H, J-J"). The first step in investigating glial-glial interactions is to establish the existence of an interaction between two cell types. The observation of the aberrant infiltration phenotype led us to a simple strategy: perturb one cell type specifically, in our case induce globular cortex glia, and assess the other subtypes for a reaction, aberrant infiltration into the cortex. Establishing a relationship between cortex glia globularity and aberrant infiltration by "other glia", any glial subtype that is not cortex glia, allowed us to establish the existence of a cortex-glia-other-glia

interaction, since the cohort of animals are genetically identical except for a cortex-glia-specific manipulation that produces globular cortex glia in the experimental cohort.

1.3 Image Quantification

1.3.1 Dataset

The dataset analyzed in this study consists of 83 confocal z-stack images capturing the ventral nerve cord of third instar, the latest of three larval stages, *Drosophila melanogaster* larvae. Confocal microscopes use a pinhole to block out-of-focus light, allowing the camera to focus in on a thin slice of the sample [59], a virtual slice. By taking images at different coordinates along the z-axis, the slices can be reconstructed into a 3-dimensional (3D) representation of the original sample. The result is similar to what is seen on a Magnetic Resonance Imaging (MRI) scan. Immunofluorescence was used to label three different cell types in different colors for each image: cortex glia, astrocytes and neuronal nuclei. In future studies, we would like to expand our focus to include interactions between cortex glia and ensheathing glia, subperineurial glia, and perineurial glia as well. However, for this study we began by concentrating on the cortex-glial-astrocyte interaction. Immunofluorescence works by using antibodies, proteins that recognize other proteins, to tag a protein of interest with a fluorophore, a compound which emits a specific wavelength of light when excited with light of a different specific wavelength [3]. By staining tissues with antibodies for proteins known to be present in certain cell types, we can visualize different cell types in different colors. Confocal microscopes house lasers of different wavelengths that are used to image the stained tissue [59]. Given that each z-stack contains approximately 30 tri-color slices, the dataset used for this study consists of approximately 7,500 single-color images.

We performed our analysis using digital images, which are essentially arrays in where each element represents the signal intensity of a pixel [60]. In the case of a single color or grayscale image, the picture would be represented as a 2-dimensional (2D) array where the X and Y dimensions align with the physical X and Y dimensions of the image. The Z-coordinate, in the case of a 3D image, and color, in the case of a multi-colored image, are represented as additional dimensions. Hence, our dataset, comprised of 3D tri-color images, was represented as 4-dimensional (4D) arrays with Z, X, Y, and color dimensions.

1.3.2 Globularity and Aberrant Infiltration Quantification

The first variable to measure in this glial-glial interaction study is globularity, which refers to the degree of change in cortex glial morphology from a reticular shape in control animals, to almost perfect spheres in animals exhibiting the strongest cortex glial change (Fig. 2.4A). We found that there was a considerable range of phenotypes in our experimental cohort, which we exploited to explore the response of other glia at different levels of cortex glial globularity rather at the two extreme morphologies exclusively. We began with a qualitative scale of cortex glial globularity, a manual globularity scale (MGS), which we used to grade cortex glial morphology with a score of 0-4, with 0 representing a completely normal morphology (Fig. 2.4A). The score is assigned based on the percentage of cortex glia that maintain a reticular shape (>95% normal cortex glia = 0, 75-95% normal cortex glia = 1, 50-75% normal cortex glia = 2, 10-50% normal cortex glia = 3, <10% normal cortex glia = 4). However, the qualitative scale raised concerns – mainly subjectivity of the grader and the large variation within each category in the scale. Measuring the intraclass correlation coefficient between three different blinded graders demonstrated the robustness of the scale, showing little variation between scores for the same image (249 images: ICC(3,k) = 0.983, $p < 0.0001$, Fig. S2.4). Unfortunately, large variation with each class remained a concern. We expected a subtle globularity-infiltration relationship, due to the large number of variables that can affect morphology in cells, which would be difficult to detect given the lack of precision in the MGS. Therefore, I explored alternatives for measuring the cortex glial morphological change. I found a strong negative correlation between the perimeter of cortex glia and its globularity as measured by the MGS (Fig. 2.4C), which allowed for the use the perimeter as a proxy for globularity. The automated morphology index (AMI, perimeter/cortex area) is a more sensitive measure that allowed us to identify more subtle patterns among a dataset with varying levels of globularity.

Quantification of aberrant infiltration into the cortex is measured by creating a region of interest (ROI) representing the cortex, and measuring the area taken up by astrocyte processes, branch-like protrusions, within this ROI (Fig. 2.5B).

1.3.3 Segmentation and its challenges

Segmentation is the process of dividing an image into foreground and background, often represented as a black-and-white or binary image. It is often a crucial step for performing tasks such as counting objects [61], measuring area and volume [62], [63], analyzing shape [64], [65], and even tracking objects in the case of video [66]. Likewise, segmentation provides the foundation for the quantification of both cortex glial globularity and astrocyte aberrant infiltration. In the case of globularity, once the cortex glia images have been segmented, their perimeter can be easily measured using established methods [67] implemented by the easy-to-use Python image analysis library scikit-image [68]. Similarly, aberrant infiltration can easily be measured by finding the overlap between a segmentation representing the cortex and another representing astrocytes.

Unfortunately, there are many factors that reduce the quality of confocal z-stacks resulting in images that are difficult to segment, which hinders the image quantification process. As discussed above, the images in this dataset were produced using immunofluorescence, which relies on fluorescently tagged antibodies. The quality of the staining produced by this technique can vary widely, even when care is taken to adhere to a protocol. Temperature and age of reagents, specificity of antibodies (to what degree they recognize only the intended protein), fixing protocol for the tissue, and other factors can all affect the fluorescent signal in the stained tissue. For the dataset used in this study, after the tissue was stained, it was imaged using a confocal microscope. As is the case with any detector collecting a signal, we expect noise will be present throughout the z-stack [69]. Additionally, the quality of the slices degrades as the distance increases from the camera due to signal attenuation [70] and convolution [71], caused by increased scattering, refraction, and absorption as light travels through thicker sections of the sample, resulting in dimmer and blurrier images respectively.

1.3.4 Segmentation Methods

Scientists and engineers have developed many methods to address the challenges that arise while producing accurate segmentations for biomedical images. Perhaps, the least technologically advanced is manual segmentation, simply tracing the outline of the intended object. Due to humans' incredible visual abilities,

this method can be very accurate, especially when done by experts. Unfortunately, this is a very expensive method in terms of person-hours, and can drastically limit the number of images that can be analyzed.

Thresholding methods are another option for segmentation. These methods rely on the assumption that foreground pixels will be brighter than background pixels. Hence, a cutoff for pixel intensity is chosen, and any pixels with a greater intensity are classified as foreground, while pixels with a lower intensity are classified as background [72]. The simplest thresholding method is to manually adjust the threshold until the resulting segmentation is satisfactory to the researcher. However, using this method to find an optimal threshold can be very tedious. More sophisticated methods apply different algorithms to the distribution of pixel intensities to select a threshold automatically, thus removing, or at least reducing, the need for human input. [72] group thresholding algorithms into different categories: histogram shape-based methods, which use information from the histogram to select the threshold; clustering-based methods, which maximize or minimize some discriminant criterion; entropy-based methods, which maximize the entropy of the resulting binary image; and object attribute-based methods, which seek to maximize similarities between the original and binary image e.g. ensuring edges coincide. Additionally, thresholding methods can be considered local or global depending on whether they consider the image in its entirety or only a small neighborhood around each single pixel respectively. Though these methods work well for relatively high-quality images, they struggle to produce satisfactory results when segmenting noisy, convoluted images. Additionally, it can be virtually impossible to select a single thresholding algorithm that performs well on all images in a dataset when there is considerable variation in the signal-to-noise ratio and degree of convolution, such as is the case in the data analyzed in this study.

In the last decades, the use of machine learning has exploded in many fields – image analysis is no exception. For the most part, image analysis makes use of supervised learning: where labeled training data is used to fit a model that can then be used to make predictions on new data [73]. Random forests, an ensemble model consisting of a group of decision trees [73], have proven to provide highly accurate segmentation results when used to classify pixels into foreground or background. Ilastik [74] and Labkit [75] are two open-source implementations of random forests for use in pixel classification. The user "paints" over sections of the image, labeling them as foreground or background. These labeled pixels are

then used to train the model such that it can classify rest of the pixels in the image [74] [75]. In our experience, classifiers created in this way do provide a highly satisfactory segmentation for the image with which they were trained. Unfortunately, as with thresholding methods, machine learning methods often lack generalizability to other images in the dataset.

Arguably the most sophisticated segmentation methods are those that use deep learning models: multi-layered interconnected structures, often artificial neural networks (ANN) [76]. As with other supervised learning approaches, ground truth in the form of a set of rigorously produced segmentations is used to train the deep models for this application [76]. Though various types of deep models have been used for image analysis tasks [77]–[79], convolutional neural networks (CNN) have shown to be particularly apt at processing images, producing highly accurate results in the hands of many groups [76] [80]–[85]. CNNs use convolutional layers to reduce the dimensionality of the input data while maintaining enough information for the ANN to perform an image analysis task [76]. There is even a variation of a CNN that was specifically adapted for work with biomedical images: U-NET. The first half of the network is a relatively standard CNN, while the second half uses upsampling to increase the resolution of the network. The reduction followed by the increase in output results in a U-shaped network. Additionally, the network contains skip-connections connecting initial layers to later, non-sequential layers which serves to utilize information about both local features, found in earlier layers, as well as more global features, found in later layers, in the final output of the network [86]. Additionally, these complex models can be highly generalizable if trained with a heterogenous dataset containing images of varying quality. The major drawbacks of deep learning methods are the relatively large, labeled datasets needed to train them, the computational power needed to fit the models, and the steep learning curve required for users to learn how to train these models [76].

1.3.5 Alternatives to Segmentation

Though some image analysis tasks do require segmentation to be accomplished, other tasks can be done in a way that does not require segmentation. In the case of this study, the most logical way of quantifying aberrant infiltration does include segmentation, since we are interested in measuring the total area, or volume, of astrocyte processes located within the cortex region. Conversely, though we chose to quantify

cortex glial globularity by measuring cell perimeter, most easily done after segmentation, I did first approach globularity quantification as an image classification problem: first by using the manual globularity score and then by attempting to automate the classification process.

Both machine learning and deep learning models are widely used to automate classification tasks in research. Generally, machine learning algorithms require data to be represented as a vector of features [73], which makes feature selection and extraction a crucial step of the process. In the case of images, each pixel intensity could be considered a feature. However, that would result in an enormous number of features, in our case $1.44X10^6$ for each single-colored slice, which would be impractical and perhaps computationally prohibitive to use in training different models. Reducing the number of features in an image into a manageable and meaningful set is a challenging task that can be approached broadly in two ways: careful and thorough examination of the data to determine important features plus creative use of non-deep-learning models, or using deep learning models to function as feature extractors and selectors [76]. For example, by reducing dimensionality while maintain important information, the convolutional layers in a CNN act as feature extractors and selectors. Both approaches have their share of challenges. Feature engineering can be a time-consuming and arduous endeavor, yet, as discussed above, training an ANNs is no trivial task.

Several teams have performed feature extraction and selection using non-deep learning methods, followed by classification with a support-vector machine (SVM), which uses hyperplanes to divide the feature vectors into different classes [73]. [87] reduce the number of features in fMRI images by limiting their focus to specific areas of the brain and performing univariate analysis of the rest of the features to determine the features with the greatest predictive power. [88] use a Bag of Features method, similar to a Bag of Words method in that the order of the features is not maintained, for feature selection of histology images. Speeded-up robust features (SURF) were extracted using the Grid selection method, and k-means clustering was used to reduce the number of features. [89] also use a Bag of Words method. They combine it with intensity order pooling for classifying human epithelia type 2 cells in a clinical setting. [90] use a multiple clustered instance learning (MCIL) method to classify cancer cell images. In multiple instance learning (MIL), the training set is composed of images that contain multiple classes, or instances. The

authors incorporate a clustering algorithm to extend MIL to MCIL, which performs classification, segmentation, and clustering simultaneously. [91] use a dual-tree complex wavelet transform (DT-CWT) for feature selection with cancer cell images. DT-CWT is a shift-invariant and orientation sensitive method for decomposing a signal into its components, or wavelets. The authors also incorporate directional difference and covariance measures into the features considered by the classifier to account for morphological variation.

Alternatively, other groups chose deep learning models to perform feature extraction. [92] built a committee machine combining an adaptive neuro fuzzy inference system (ANFIS) and a feed-forward neural networks (FFNN) to classify images of the retina for diagnostic purposes. ANFIS learn a set of if-then fuzzy rules that are later used to classify observations. FFNN only have connections between consecutive layers, and the signal only travels forward. As previously discussed, though ANNs have proved successful as feature extractors and feature extractor/classifiers, they require very large, labeled datasets to be trained. Such large training sets are often not available in life science research and clinical settings. In these cases transfer learning, adapting pre-trained networks to perform a similar but different task, can be useful, since they allow for the use of deep learning with a smaller training set [93]. [94] modified a convolutional neural network (CNN), pretrained on ImageNet, a large collection of non-medical images, for classifying photographs of plant diseases. [95] used a pre-trained network both as purely a feature-extractor and as a feature-extractor/classifier for histopathology images. [96] used a pre-trained CNN as a feature extractor in conjunction with an SVM to classify mammograms for breast cancer diagnosis. Similarly, [93] used a pre-trained CNN and an SVM to classify their images, inner ear images used to diagnose inflammation and inner ear disorders. Finally, [97] modified a pre-trained CNN for classifying images of brain MRIs for diagnostic purposes.

For an initial attempt at automating the quantification of cortex glial globularity, I used transfer learning to adapt a pre-trained CNN to classify cortex glial globularity according to the manual globularity scale (Fig 1.1). As the base, I used MobileNetV2, a CNN specifically engineered to reduce the amount of computational power needed for training [98], pre-trained on the ImageNet dataset. I used a training set of 1221 pre-segmented, manually-scored, single-channel, 2D, cortex glial images. The training set was

11

augmented into 9760 images by using transformations, such as rotating and flipping, as discussed in [94]. I split the labeled set into a training (70%), validation (15%), and testing set (15%). Briefly, I used the training and validation set to refit either the top layer (Fig. 1.1B-B') or the top 55 layers of the network (Fig. 1.1C-C'), adjusting the model to classify cortex glial images instead of the ImageNet images, and the testing set to assess the performance of the model. The top accuracy reached by the model, when adjusting the top 55 layers, was ~55% (Fig1.1C, code in Appendix).
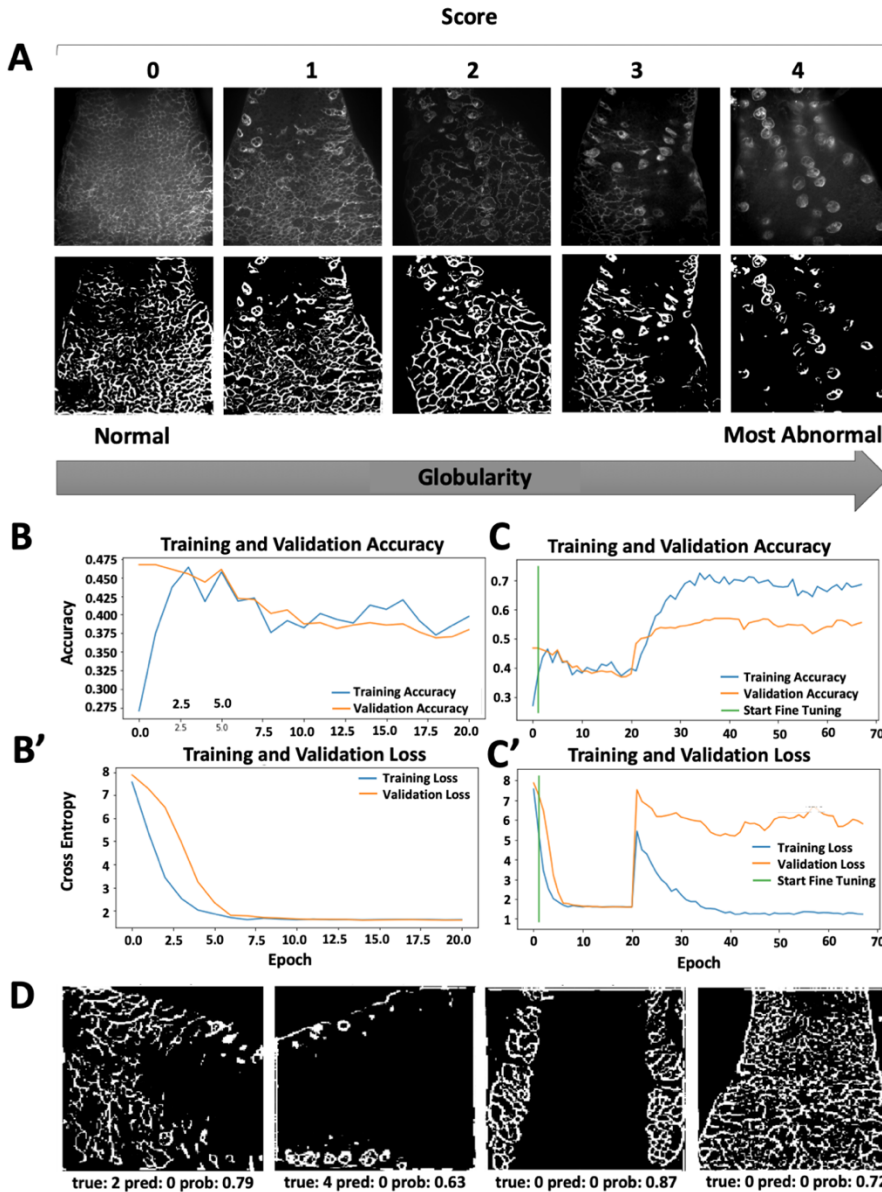
Fig. 1.1: Quantification of Cortex Glia Globularity Using Transfer Learning to Adapt Pretrained MobileNetV2.

Model was trained using RMSProp. Sparse categorical crossentropy was used as the loss function. (A) Training Data: Representative images for each cortex glial globulariy class. Binary images were used in training. (B) Training Top Layer: Base model layers were frozen during training of top layer. (C) Fine-tuning: Top 55 layers of base model were unfrozen and trained. (D): Adapted Model Predictions Examples: True label (true), model's prediction (pred), and model's calculated probability (prob) for the prediction.

1.3.6 Image Analysis Pipeline Overview

The low accuracy of the CNN prompted me to find an alternative way to quantify cortex glial globularity. I found that perimeter is a suitable proxy for globularity. Using perimeter as a globularity measure also has the considerable advantage that it provides a much more precise measurement than grouping cortex glial morphology into five classes. Hence, my focus shifted from developing a classifier for cortex glial globularity to finding a way to accurately segment cortex glia, in addition to finding segmentation algorithms for the cortex region and astrocytes to be used for the quantification aberrant infiltration,

Due to the computational power requirement, the need for large, labeled training data sets, and higher level of expertise needed to fit more sophisticated models, I sought to use the simplest models possible that would not require a high degree of human input, which would be impractical for quantifying the large dataset used in this study. The scikit-image library provides a large collection of functions that perform denoising and thresholding using different algorithms. I tried various combinations of denoisers and thresholders on a subset of images, and found that though there was no single denoising/thresholding combination that segmented all images satisfactorily, I was able to successfully segment all images with one of the combinations. The final image analysis pipeline selects the best segmentation algorithm from a small number of options, and uses the resulting cortex glia, cortex region and astrocyte segmentations to quantify cortex glial globularity and aberrant astrocyte infiltration respectively (Fig. 2.2).

Chapter 2: Quantifying glia-glial tiling using automated image analysis in *Drosophila*

2.1 Abstract

Not only do glia form close associations with neurons throughout the central nervous system (CNS), but glial cells also interact closely with other glial cells. As these cells mature, they undergo a phenomenon known as glial tiling, where they grow to abut one another, often without invading each other's boundaries. Glial tiling occurs throughout the animal kingdom, from fruit flies to humans; however, not much is known about the glial-glial interactions that lead to and maintain this tiling. *Drosophila* provide a strong model to investigate glial-glial tiling, where tiling occurs both among individual glial cells of the same subtype, as well as between those of different subtypes. Furthermore, the spatial segregation of the CNS allows for the unique ability to visualize and manipulate inter-subtype interactions. Previous work in *Drosophila* has suggested an interaction between cortex glia and astrocytes, where astrocytes cross the normal neuropil-cortex boundary in response to dysfunctional cortex glia. Here, we further explore this interaction by implementing an automated pipeline to more fully characterize this astrocyte-cortex-glia relationship. By quantifying and correlating the extent of cortex glial dysfunction and aberrant astrocyte infiltration using automated analysis, we maximize the size of the quantified dataset to reveal subtle patterns in astrocyte-cortex glial interactions. We provide a guide for creating and validating a fully-automated image analysis pipeline for exploring these interactions, and implement this pipeline to describe a significant correlation between cortex glial dysfunction and aberrant astrocyte infiltration, as well as demonstrate variations in their relationship across different regions of the CNS.

2.2 Introduction

Neurons and glia comprise the majority of the cells in the central nervous system (CNS). We often think of neurons as having the main function—signal transmission—whereas glia perform a variety of supportive duties. Glia sculpt neurons during development and plasticity [99]–[102], engulf debris in development, injury, or disease [103]–[106], provide neurons with key nutrients and metabolic support [100], [107]–[110], ensheath axons for proper axonal conduction and integrity [111]–[113], maintain the blood brain barrier [114]–[117] and buffer ions and neurotransmitters to modulate neuronal activity [46], [118], [119].

Given the wide range of these and additional functions, it is not surprising that glia have been shown to play roles in a number of neurological disorders such as Autism, Epilepsy, Schizophrenia, as well as neurodegenerative disorders like Alzheimer's disease [38], [120]–[123]. Thus, elucidating glial function is a crucial step in achieving a thorough understanding of the brain.

In addition to interacting extensively with neurons, glia also form complex physical and signaling interactions with each other. One of the ways in which glial-glial interactions manifest is a phenomenon known as tiling, where each glial cell grows to fill a space without invading the boundaries of others. Many glial cells form almost perfectly tiled domains that exhibit very little overlap between cells; however, the exact amount of overlap between these glial domains can vary between species, age, and disease state [43]–[45]. Tiling can be observed between glia of the same subtype, such as between two or more astrocytes [42], [47], [124], microglia [48], oligodendrocyte precursor cells [125], Müller glia [126] as a few examples, as well as between glia of different subtypes [40], [117], [127]. Importantly, glial tiling and domain organization is highly conserved among species from flies to humans [43], [127]; however, little is known about the interactions that lead to and maintain glial tiling in any species. Moreover, the functional relevance of this tiling remains almost completely unexplored.

As a model, *Drosophila melanogaster* strikes a balance between simplicity and complexity that makes it especially suitable for conducting a thorough examination of glia-glial interactions. Despite its simplicity, the fly CNS maintains a high degree of complexity, composed of multiple neuronal and glial subtypes that share cellular, genetic, and functional conservation with their mammalian counterparts [25], [56]. Furthermore, because of the high level of genetic, proteomic, signaling, and cellular conservation from flies to mammals, many findings made using *Drosophila* are applicable to understanding the mammalian brain [57]. The elegance of *Drosophila* genetics has allowed for the development of a vast and powerful arsenal of genetic tools that makes this an attractive model for investigating glial tiling [25] [57], [58]. Specifically, these tools allow for genetic labeling and manipulation of either single cells or entire cell-type populations, as well as applying different genetic alterations to multiple cell types at the same time (Fig. 2.1).
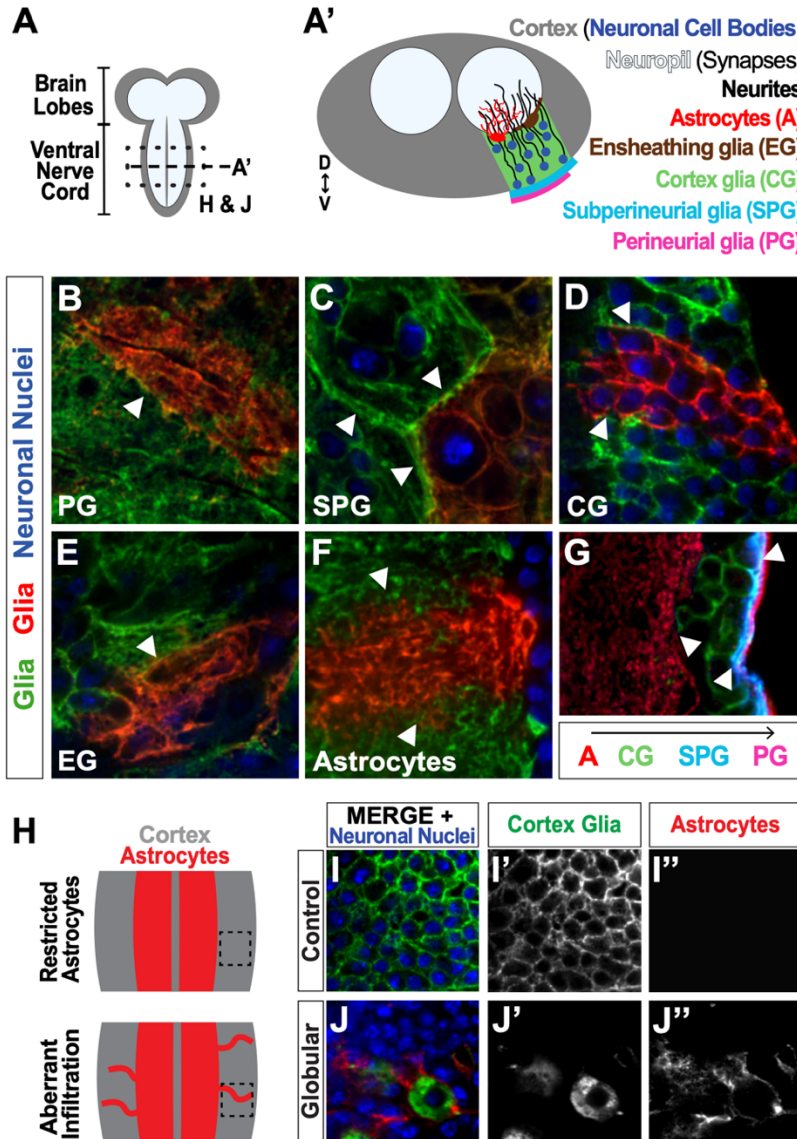
Fig. 2.1: Drosophila serves as a strong model for investigating glial tiling.

(A) Schematic of the *Drosophila melanogaster* larval central nervous system (CNS), subdivided into the cortex (gray, containing the cell bodies) and the synaptic neuropil (white). (A') Cross-section of the ventral nerve cord (VNC) depicting neuronal nuclei (blue) and single cell examples of different glial subtypes to show their distinct spatial segregation: Perineurial glia (PG, magenta) and subperineurial glia (SPG, cyan) form a barrier around the CNS, cortex glia (CG, green) wrap neuronal cell bodies, and ensheathing glia (EG, brown) and astrocytes (red) are associated with the neuropil. (B–F) Tiling between cells of the same glial subtype shown in green and red with neuronal nuclei shown in blue: PG (B, surface view), SPG (C, surface view), CG (D), EG (E, surface view), astrocytes (F). (G) Tiling between different glial subtypes: PG (magenta), SPG (blue), CG (green), astrocytes (red). Examples of tiling boundaries depicted with white arrowheads. (H) astrocyte aberrant infiltration (red) into the cortex (gray) upon disruption of CG morphology. (I,J) Images corresponding to black inset in (H), showing control (I) and globular (J) cortex glial conditions, where astrocytes can be seen infiltrating the cortex in (J"). Cortex glia in green (I',J'), astrocytes in red (I",J"), neuronal nuclei in blue.

The spatial organization of the *Drosophila* CNS makes this a particularly ideal model for studying glial-glial tiling (Fig. 2.1A-A'). The *Drosophila* CNS is subdivided into two main regions, the cortex and neuropil, where the cortex comprises the neuronal cell bodies and the neuropil contains the synapses. Furthermore, the CNS contains multiple glial cell types that spatially segregate along these regions, and are known to tile within and between subtypes. Perineurial glia (PG, Fig. 2.1A', surface view in Fig. 2.1B), and subperineurial glia (SPG, Figure 2.1A', surface view in Figure 2.1C) wrap the CNS to form the blood-brain

barrier [115], [116] [25], [117] [128]. Cortex glia (CG, Fig. 2.1A',D) intersperse among the neuronal cell bodies in a mesh-like pattern to wrap and support the somas [25], [128], where each cortex glial cell wraps 50–100 neuronal cell bodies [40], [127], providing metabolic support [108], and debris clearance in the cortex [40], [106]. Ensheathing glia (EG, Fig. 2.1A', surface view in Fig. 2.1E) and astrocyte cell bodies are located on the interface between the cortex and neuropil [25], [128], where EG processes form a barrier between the two regions [129], and astrocytes extend fine processes into the neuropil (Fig. 2.1A',F) that interact with synapses [102] [46] [118] [124]. Each of these subtypes forms tight boundaries between cells of their own kind [40], [124], [127], [129], as well as between different glial subtypes such as astrocytes and cortex glia, cortex glia and SPG, or SPG and PG (Fig. 2.1A',G) [40], [117], [127]. We have previously shown that upon morphological disruption of cortex glia caused by the loss of the neurotrophin spätzle 3 (Spz3) or soluble NSF attachment protein α (αSNAP, part of the vesicular fusion machinery the vesicular fusion machinery that leads to Spz3 secretion), neuronal cell bodies lose their physical interactions with cortex glia, and astrocytes extend aberrant processes into the cortex (Fig. 2.1H–J) [40]; however, the previous report found that this phenomenon occurs, but did not quantify the extent to which it occurs or the relationship between the degree of cortex glial morphological disruption and aberrant astrocyte outgrowth.

In an effort to more fully characterize the tiling relationship between cortex glia and astrocytes, and to further establish this model for investigating the disruption of glial-glial tiling, we sought to implement an automated analysis of the extent of globular morphological transformation of cortex glia and astrocyte infiltration, and assess the relationship between the two characteristics. Here we describe a method for creating and validating an automated image analysis pipeline using free, open-source software. Using this optimized pipeline, we reveal a significant correlation between the extent of cortex glial morphological disruption and aberrant astrocyte infiltration. Additionally, these data allow us to explore regional variations in morphology and infiltration throughout the dorsal-ventral axis of the CNS.

2.3 Materials and Tools

2.3.1 Fly Strains

Drosophila melanogaster crosses were raised at 29∘C on Nutri-fly Molasses Formulation food (Genesee Scientific). The following previously made transgenes were used in this study: *Wrapper932i-LexA* (Driver

1) [40], *CtxGliaSplit-Gal4* (Driver 2) [40], *GMR54H02-Gal4* (BDSC 45784)*, alrm-Gal4* (with Driver 1) [130]*, alrm-LexA::GAD* (with Driver 2) [124], *GMR56F03-Gal4* (BDSC 39157), *GMR85G01- Gal4* (BDSC 40436)*, GMR54C07-Gal4* (BDSC 50472), *Mi{PT- GFSTF.0}trolMI04580-GFSTF.0* (BDSC 60214), repoFLP, *UAS- CD8>GFP>RFP* [124], *UAS-αSNAPRNAi* (VDRC 101341)*, LexAop2-Spz3RNAi* [40]*, UAS- CD8::GFP* [131]*, UAS-CD8-mCherry* [124], *LexAop-rCD2::GFP* [132]*, and LexAop-rCD2::RFP* [132].

2.3.2 Immunohistochemistry and Imaging

The larval CNS was dissected in the third instar larval stage. The samples were fixed in ice-cold 100% methanol for 5 min at room temperature, then rinsed three times with PTX (PBS + 0.1% Triton-X). Samples were stained overnight with primary antibodies at 4°C, rinsed three times with PTX, then stained overnight with secondary antibodies at 4°C. The following primary antibodies were used: chicken anti-GFP (1:1000; Aves Labs), rabbit anti-dsRed (1:500; Clontech), rat anti-Elav (1:100; Developmental Studies Hybridoma Bank, 7E8A10), rabbit anti-GAT (1:2000) [124], rat anti- CD2 (1:500; Bio-Rad). The following secondary antibodies were used: donkey conjugated to DyLight 488 [anti-chicken (103- 005-155)], Cy3 [anti-rabbit (711-165-152)], and Cy5 [anti-rat (712-175-150)] from Jackson ImmunoResearch. After washing three times with PTX, samples were mounted in VectaShield reagent (Vector Laboratories) and imaged on an Intelligent Imaging Innovations (3i) spinning disk confocal microscope equipped with a Yokogawa CSX-W1. Finally, out-of-focus images from the beginning or end of the stack were removed. A total of 3,309 images from 84 three-channel confocal Z-stacks marking astrocytes (red channel), cortex glia (green channel), and neuronal cell bodies (blue channel) were analyzed.

2.3.3 Image Processing and Automated Pipeline Analysis

This pipeline was specifically designed to take advantage of open-source software that allows for its implementation by nearly anyone with access to two-dimensional images. Importantly, it does not require access to more expensive three-dimensional imaging capability like light sheet microscopy or specialized 3D image analysis software licenses, making this tool easy for almost anyone to implement to maximize their analyses and reduce unintentional bias that can occur with manual quantification. Briefly, following

preprocessing, the images were fed into the pipeline, separated into individual single-channel 2D-images and denoised. The images were then thresholded to produce binary images, and simultaneous scoring occurred for both globularity and infiltration. Cell perimeter was used as a proxy for quantifying cortex glia morphology, while aberrant astrocytic process infiltration was quantified by measuring the overlap between the astrocyte channel and the cortex, determined by combining the cortex glial and neuronal channels. Finally, the scores produced by pipeline were analyzed to assess the relationship between cortex glia morphology and aberrant infiltration by astrocytes (Fig. 2.2). Scikit-image [68] was used for all automated image processing and analysis. Manual image quantification for automated score validation was performed using FIJI/ImageJ [133].
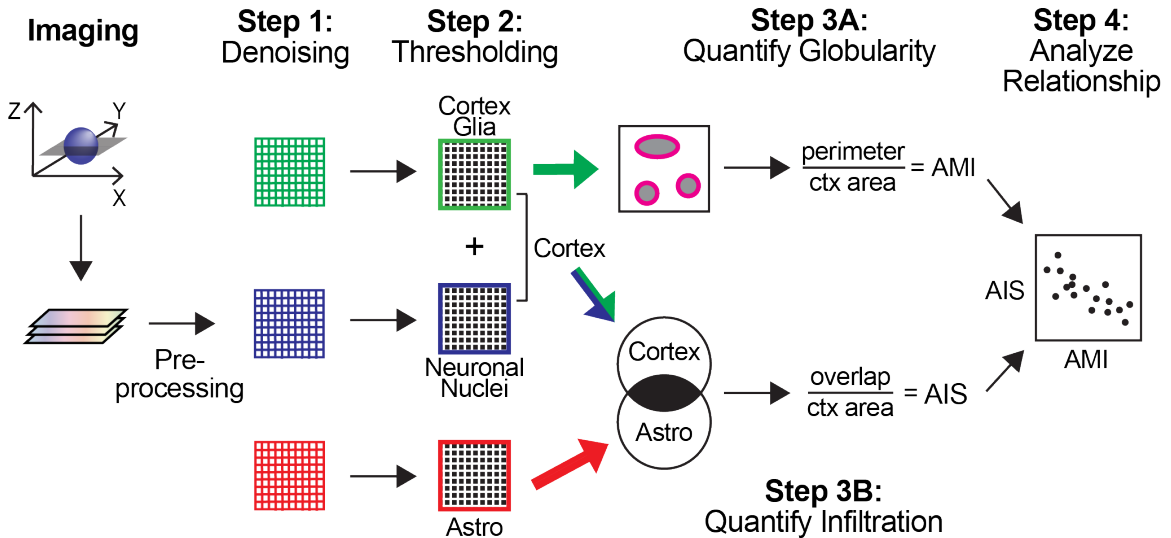
Fig. 2.2*: Schematic of automated image analysis pipeline for 3-channel confocal Z-stacks.*
Preprocessing: Z-stacks were separated into 2D arrays representing a single plane for each cell type (corresponding to a single channel for each). Step 1: Individual channel images were denoised. Step 2: 2D arrays were thresholded to produce binary images. Step 3A: The perimeter of cells in the cortex glia (CG) channel was measured and normalized to total cortex area producing an automated morphology index (AMI) score. Step 3B: CG and neuronal nuclei channels were combined to define the cortex area (ctx). The overlap between the ctx and astrocyte (astro) channels was calculated and normalized to the total cortex area to produce an automated infiltration score (AIS). Step 4: The relationship between the AMI and AIS was analyzed.

Denoising removes noise generated by factors such as light scattering and signal attenuation, and aids in generating more accurate binary representations of the raw image (Fig. S2.1). Compared to the original image (Fig. S2.1A), unsharp masking with scaling amount 2 and radius 20 produced the optimal image to identify astrocyte processes (Fig. S2.1B, red outline), where the sharpened image is produced by scaling (multiplying by the scaling amount) the difference between the original image and an image

generated by adding noise in a radius-parameter- defined distribution [134]. The same parameters were used for denoising the cortex glial channel, and the neuronal channel parameters were set to 3 and 20 for the scaling and radius, respectively. Other parameter values either failed to identify all astrocyte processes (Fig. S2.1B) or added undue noise (Fig. S2.1C) that would interfere with infiltration analysis in further steps of the pipeline. Denoised images are only approximations; therefore, to ensure accurate scoring by our pipeline, we included validation steps comparing results obtained by manual quantification with those obtained in an automated fashion (Fig. 3–5).

Denoised images were then subjected to thresholding to convert grayscale to binary images, with the algorithm-selection process performed separately for each channel. Local algorithms, which consider only a pixel's nearest neighbors [72], were eliminated as possible candidates due to their poor performance, as judged by a qualitative comparison of the original and binary image. Second, 68 denoised images of the channel in question were binarized with seven global thresholding algorithms, where the image as a whole is used to calculate a thresholding limit (Fig. S2.2A) [72]. For each of the sample images, a visual comparison of the original and binary image was used to determine the top three algorithms. The top algorithm was assigned a score of 3, the second-place algorithm was assigned a score of 2, and the third was assigned a score of 1. All other algorithms received a score of 0, and ties in this scoring were allowed. The final score for each algorithm was the sum of the scores for all the sample images. No single thresholding algorithm yielded satisfactory results for 100% of the sample images. We therefore implemented a decision tree into our pipeline to choose among the best thresholding algorithms for each channel in each image. We classified unsatisfactory results as those producing blown out images that contained superfluous signal or blacked out images where true signal was removed (Fig. S2.2B). First, the pipeline determines whether the image produced by Otsu's method [135] is blown out by exploiting the difference in texture between noise and true signal. Neuronal cell bodies have the appearance of distinct circles. Noise has the appearance of smaller, more densely and evenly distributed specks. Additionally, in blown out images, the majority of the noise being misrepresented as true signal was located in approximately the middle third of the image, the section corresponding to the neuropil. We converted all contiguous white objects smaller than 75 pixels to black, effectively removing specks, and the middle third
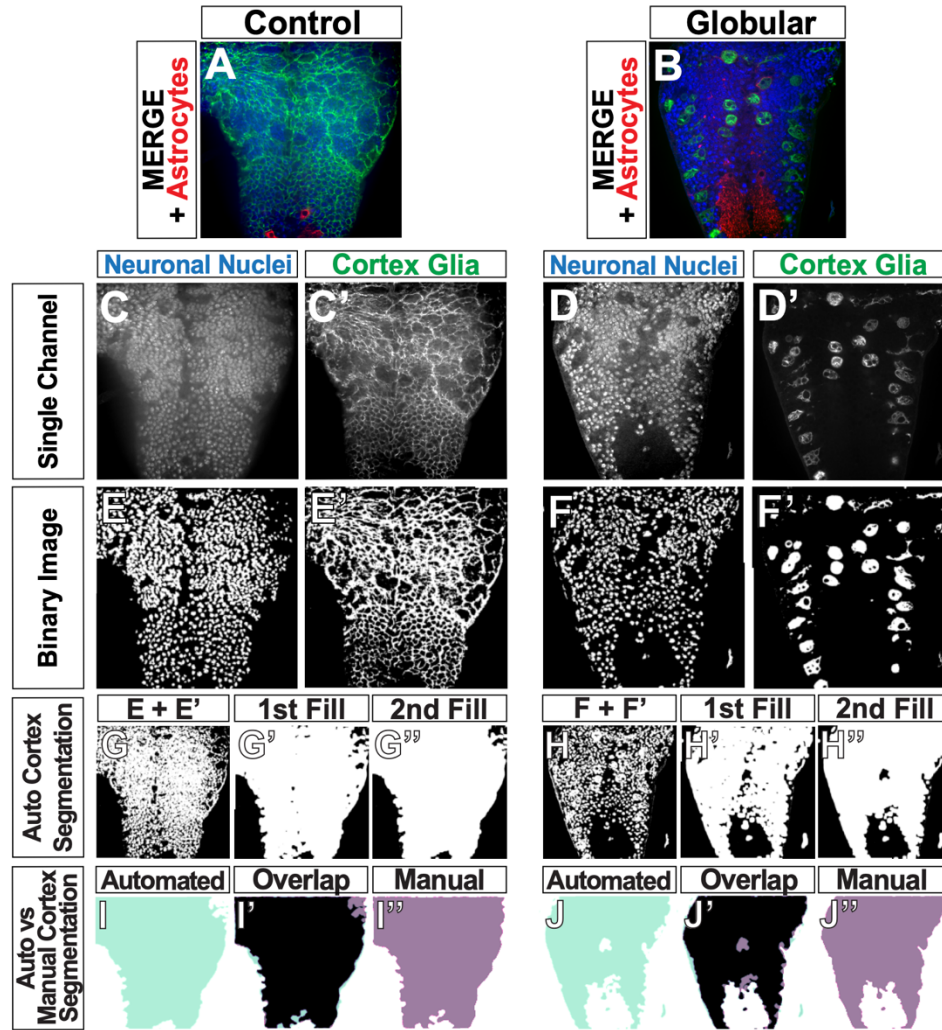
Fig. 2.3: Automated determination of the cortex region.

(A,B) Original images of control (A) and globular CG (B) consisting of three channels: CG (green), neuronal nuclei (blue), and astrocytes (red). (C–F) Gray scale images of single channels (C–D') were converted binary images (E–F'). (G–H") Binary images of neuronal nuclei and CG were then combined to define the cortex (G,H). Gaps between the nuclei and CG membranes were filled to produce solid white area covering the entire cortex (G',G",H',H"). (I–J") Comparison of the cortex segmentations obtained by the automated pipeline (aqua, I,J) and by manual tracing of the same image (purple, I",J"), with the overlap depicted between the two in black (I',J', black).

of the image was then compared before and after despeckling. If despeckling resulted in a 7% or greater

reduction in the number of white pixels, the image was determined to be blown out, and the Triangle

algorithm [136] was used to threshold the image. Conversely, if the pipeline assessed that the binary image

was blacked out, i.e., less than 2% of pixels were white, the pipeline will choose the Li thresholding

algorithm [137], [138] instead of Otsu's method. A similar process was used to implement decision trees

for selecting thresholding algorithms for the cortex glia and astrocyte channels. For cortex glia, the pipeline

chooses between the Otsu and Triangle algorithms. For astrocytes, the pipeline chooses between the Otsu,

Triangle and Yen [139] algorithms.

After the pipeline generates binary images for each channel (Fig. 2.3E,F) using its selection of

optimal algorithms, we perform a segmentation, or detection of the cortex by combining the neuronal

nuclei and cortex glia binary images and adjusting the result (Fig. 2.3G,H). Merely combining the two

channels results in a cortex segmentation that is not completely solid (Fig. 2.3G',H') due to gaps between

the visualized neuronal nuclei and the cortex glia membrane, representing the rest of the neuronal cell body

and cytoplasm. Since aberrant infiltration is quantified as the overlap between the cortex and astrocytes, a

cortex segmentation with these gaps is likely to result in an undercount of infiltration. Hence, segmentation

of the cortex was performed in four steps: merge (Fig. 2.3G,H), 1st fill (Fig. 2.3G',H'), 2nd fill (Fig.

2.3G",H") and a final finetuning step. The sequential fills were executed by our implementation of a

dilation algorithm [140], in which a black pixel was turned white if >10% of the neighbors within a 15-

pixel radius were white, followed by Scikit-image's remove_small_holes function [68], which turns to

black any contiguous white objects smaller than set radius (5,000 pixels in our pipeline). Since the resulting

segmentation was slightly larger than the true cortex region, an erosion algorithm— where a white pixel

was turned to black if any of its immediate neighbors was black [140]—was used to reduce the size of the

segmented area.

2.3.4 Automated Cortex Segmentation Validation

The functions used for automatically segmenting the cortex required a total of four parameters to be set:

neighborhood (n) and threshold for the first fill step (thresh), hole size (hole_size) for the second fill, and

the number of erosions (erosions) to finetune the segmented region size. In order to optimize values for

these parameters, we compared the cortex region segmented in an automated fashion (automated, light

green) to those produced manually (manual, purple) (Fig. 2.3I,J). We used two metrics to determine the

accuracy of the pipeline (Fig. S2.3): overlap (OL) divided by the manually segmented region (OL/M) and

OL divided by the automatically detected (A) cortex (OL/A). A high OL/M score indicates that the pipeline

is capturing a high percentage of the manually segmented region, interpreted as a high true positive rate. A

high OL/A score indicates that the pipeline is not erroneously capturing areas that were not part of the

manual segmentation, and can be thought of as low false positive rate. We used 42 images to test 192 different combinations of the four ROI-selection parameters (3–4 values per parameter, Fig. S2.3A). We chose the parameter set with the highest OL/M and OL/A scores (Supplementary Figure 3B, n = 15, thresh = 0.10, hole_size = 5000, erosions = 10, mean OL/M = 88.21%, mean OL/A = 85.46%). OL/M and OL/A scores of 100% would indicate a perfect overlap between the manual and automated ROIs. We would expect some small amount of error in the manual scores due to difficulty tracing a perfect outline of the cortex (given noise in images, limitations in image resolution, etc.). The majority of the scores lie above the mean, indicative of a highly accurate automated cortex detection method.

2.4 Results

2.4.1 Quantification of Cortex Glial Morphology

While cortex glial morphology is altered upon the loss of Spz3 or αSNAP, there can be variation in the degree of cortex glial globularity after genetic manipulation (Fig. 2.4A). We automated the scoring of cortex glia morphology by utilizing the perimeter of the cells as a proxy for globularity (Fig. 2.4B). As cells become more globular, there is a drastic reduction in their perimeter. The automated morphology index (AMI) for each image is calculated as the total perimeter of the cells, normalized by the total area of the cortex, and expressed as a percentage of that area.

As with cortex segmentation validation, we assessed AMI accuracy by comparing automated scores with manually obtained scores for the same images. For manual scoring, cortex glia images were assigned a manual globularity score (MGS) of 0–4 (Fig. 2.4A). AMI and MGS are significantly negatively correlated (Fig. 2.4C, $p < 0.0001$, $r^2 = 0.47$), where a lower AMI indicates a greater morphological change. MGS was validated by comparing scores generated by three different blinded researchers for the same images, and finding a very high level of agreement between the scores as calculated by the intraclass correlation coefficient [249 images: ICC(3,k) = 0.983, $p < 0.0001$, Fig. S2.4]. When MGS scores were sorted by experimental group, the same patterns were revealed by MGS (Figure 4D) and AMI (Fig. 2.4E, *y*-axis flipped for ease of comparison to Fig. 2.4D). The no-RNAi control condition exhibited the lowest cortex glia globularity, indicative of normal morphology, followed by a LexA-driven knockdown of Spz3 (driver 1), and then a Gal4-driven knockdown of αSNAP (driver 2) with the highest globularity scores.

23

These drivers specifically allowed us to explore variable morphological changes, as driver 1 is weaker than driver 2, which exhibited the highest variation in morphology. All pairwise comparisons of the groups are highly significant for both the manual and automated scores ($p < 0.001$, pairwise *post hoc* Dunn's test), indicating that the pipeline is accurate in quantifying morphology.
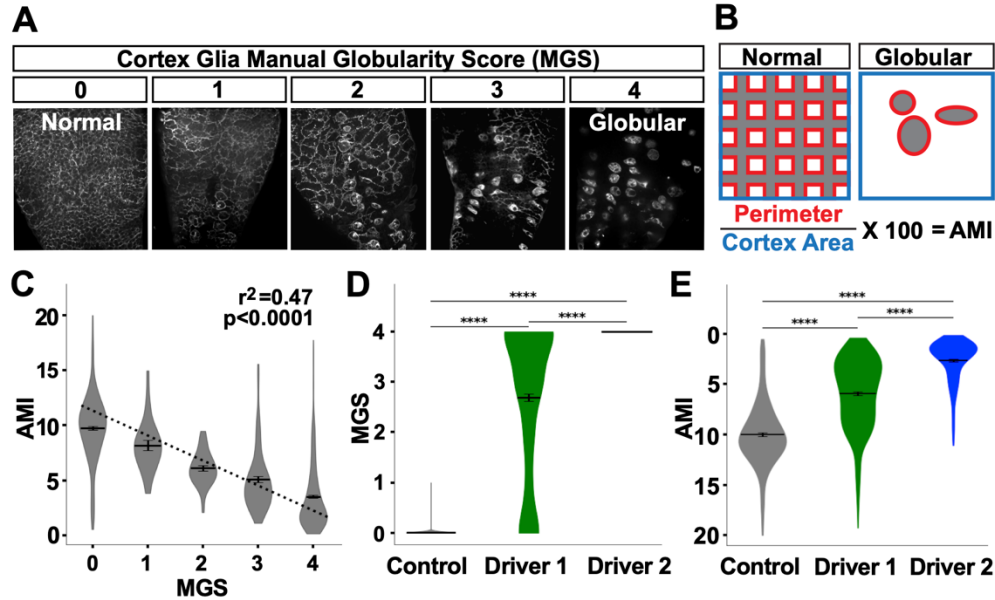
Fig. 2.4: Automated morphology index (AMI) significantly correlates with manual scores for cortex glial globularity.

(A) Cortex glial morphology was manually quantified using a 0–4 range, with 0 being normal mesh-like morphology, and 4 being almost completely globular (manual globularity score, MGS). (B) The automated morphology index (AMI) was calculated in the pipeline by measuring the perimeter of the cortex glia divided by the total area of the cortex. (C–E) AMI and MGS shows a significant negative correlation (C, $p < 0.0001$, $r^2 = 0.47$, dotted line denotes the regression line). As globularity increases after RNAi knockdown using driver 1 (weaker) or driver 2 (stronger) (D), the AMI decreases (E, inverted *y*-axis for ease of comparison to MGS). ****$p < 0.0001$.

2.4.2 Quantification of Infiltration by Astrocyte Processes

Once the cortex has been segmented, the overlap between the cortex and astrocyte channel is measured in pixels and expressed as a percent of the total cortex area (Fig. 2.5A,B). Astrocyte morphology introduces a complicating factor in quantifying infiltration, as astrocyte cell bodies are located within the cortex on the edge between the cortex and neuropil, as indicated by the circles in Fig. 2.5A (red) and Fig. 2.5B (dark red). However, these cell bodies do not constitute aberrant infiltration, and therefore need to be removed from the pipeline data to be quantified (outlined in red squares in Fig. 2.5C'). Using the ratio of foreground to

background pixels within the box bounding an object [141], the roundness of an object [142], and area, we defined and excluded objects that are cell bodies while preserving aberrant infiltration (Fig. 2.5C–C'").
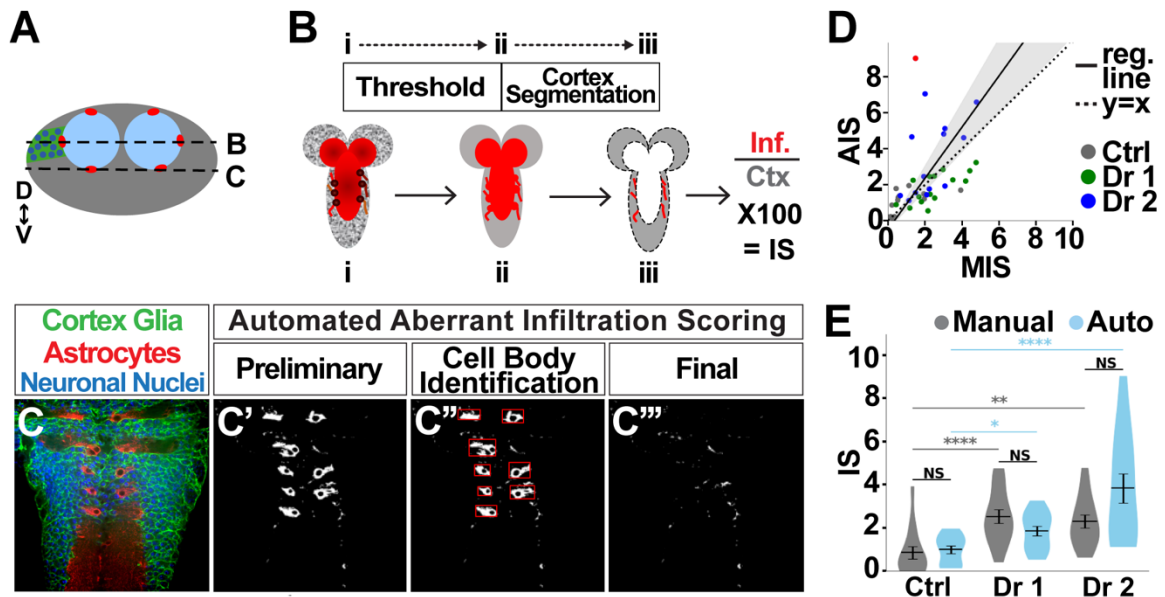

Fig. 2.5: Automated quantification of astrocyte infiltration.
(A) Cross section of the VNC depicting the location of astrocyte cell bodies, as well as the location of longitudinal sections shown in **(B,C)**. **(B)** Images were taken in longitudinal planes. The astrocyte channel was then thresholded, and the area of overlap between astrocytes and the cortex region was quantified as the infiltration score (IS). **(C)** Astrocyte cell bodies reside in the cortex under normal conditions **(C')**, but were identified **(C")** and excluded from the quantification to identify only aberrant cortex infiltration **(C'")**. **(D)** Manual vs. automatic (auto) scores significantly correlate (95% confidence interval depicted by gray shaded area), with control (gray), driver 1 (green), and driver 2 (blue), (slope = 1.424, 95% CI [1.076, 1.772], $r^2 = 0.22$, $p < 0.0001$, $n = 42$). Only one point was identified with a difference of greater than 6 (red) between manual and automated scores. **(E)** There is no significant difference between manual and automated scores for any of the groups. Pairwise comparison using Kruskal–Wallis test. NS $p > 0.5$ (control $p = 0.343$, driver 1 $p = 0.678$, driver 2 $p = 0.155$). $p < 0.001$ for Kruskal–Wallis test comparing three groups with same scoring methodology, followed by Dunn *post hoc* pairwise comparisons. *$p < 0.05$, **$p < 0.01$, ****$p < 0.001$. Control $n = 14$, KD driver 1 $n = 15$, KD driver 2 $n = 13$.

As with automating the morphological assessment of cortex glia, validating automated astrocyte infiltration scores is a critical step. By comparing 43 images using both methods, we found a highly significant correlation ($p < 0.0001$, $r^2 = 0.22$) between the manual and automated infiltration scores (MIS and AIS, respectively). A correlation between perfectly matching sets of scores would be indicated by a slope of 1 (Fig. 2.5D dotted line). We found an AIM vs. AIS correlation with slope = 1.424 95% CI [1.076, 1.772] (Fig. 2.5D, solid black line surrounded by shaded gray region). There is a single case in which there was a discrepancy between the manual and automated scores of ±6 (red dot in Fig. 2.5D). Without this point, which represents only 2.22% of the images considered in this validation procedure, the correlation slope is 1.19

95% CI [0.933, 1.452]. As part of AIS validation, we also examined automated scores for systematic errors in scoring, and found there is no experimental group for which the points lie solely on one side of the regression line (Fig. 2.5D). Furthermore, scores pooled per experimental group and quantification method (Fig. 2.5E) show no significant differences between AIS and MIS (pairwise Kruskal–Wallis comparisons, control $p = 0.343$, driver 1 $p = 0.678$, driver 2 $p = 0.155$). Finally, the two scoring methodologies indicate the same shifts in aberrant infiltration. Controls have the lowest infiltration, driver 1 shows intermediate infiltration, and driver 2 exhibits the greatest infiltration. Significant differences between scores obtained using the same methodology are color-coded: gray for manual scoring, blue for automated scoring (Kruskal–Wallis test followed by Dunn pairwise comparisons. $^*p < 0.05$, $^{**}p < 0.01$, $^{***}p < 0.001$). Taken together these data demonstrate that infiltration scores using the automated pipeline are accurate.

2.4.3 The Relationship Between Cortex Glial Morphology and Aberrant Astrocyte Infiltration

Scores for all images in the CNS were averaged to determine global scores for each animal for AMI (Fig. 2.6A) and AIS (Fig. 2.6B). These global scores were used in assessing the relationship between cortex glial morphology and astrocyte infiltration (Fig. 2.6C). Correlations between AMI and AIS scores were assessed using Spearman's rank correlation coefficient to allow for the possibility of a non-linear relationship between cortex glial globularity and aberrant astrocyte infiltration. Interestingly, not all areas of the CNS appeared to be equally affected, with apparent heterogeneity in both AMI and AIS along the dorsoventral axis. In order to explore the possibility of location-dependent heterogeneity in morphology and infiltration, we divided the CNS into three zones along the dorsal-ventral axis (Fig. 2.7A), with the ventral surface set to a z-coordinate of 0 and the dorsal surface to 100. Differences in AMI and AIS were explored using a sliding window to analyze 10% of the total CNS depth at a time (Fig. 2.7B,C). Scores for all images within each 10% window belonging to a single stack were averaged to produce a local dorsal-ventral depth score represented as mean ± SEM. AMI was higher throughout the CNS in the controls compared to either driver knockdown condition
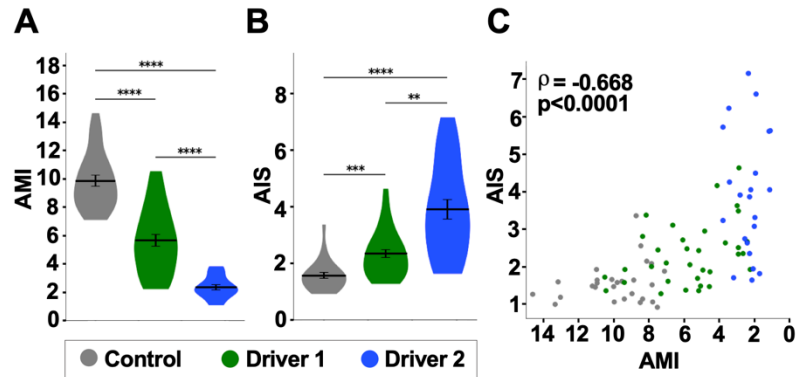
Fig. 2.6: Astrocyte infiltration significantly correlates with disrupted cortex glial morphology.
(A,B) As cortex glial (CG) morphology becomes more impaired, shown by reduced automated morphology index (AMI, in A), the automated astrocyte infiltration score (AIS) increases (B). Kruskal–Wallis test comparing all groups, followed by Dunn *post hoc* pairwise comparisons. **$*p < 0.01$, ***$p < 0.001$, ****$p < 0.0001$. (C) AIS and AMI are significantly correlated, as indicated by Spearman's rank correlation coefficient ($\rho = -0.668$, $p < 0.0001$). Scores for individual images of each CNS were grouped and averaged by animal. Control $n = 27$, Driver 1, $n = 34$, Driver 2 $n = 22$ animals.

($p < 0.0001$ for Kruskal–Wallis test comparing all groups, ****$p < 0.0001$, ***$p < 0.001$ with Dunn's pairwise comparisons). AMI was lowest in the middle of the VNC, at approximately 40–50% along the dorsal-ventral axis. Average AIS was also higher throughout the VNC for knockdown animals; however, the inter-group difference in AIS was less pronounced than that of AMI. Driver 1 showed little to no difference in infiltration scores in the ventral 20% of the VNC. Additionally, there was only a modest increase in infiltration in the top 10–20% nearest the dorsal surface for animals in the driver 1 group. The largest increase in infiltration scores for these animals was found in the middle 50–80% of the VNC. In contrast, driver 2 showed the largest increase in infiltration near the surface of the VNC, at both ventral and dorsal ends, with a more subtle increase in the middle of the VNC.

The correlation between local AMI and AIS was calculated using Spearman's rank correlation coefficient (Fig. 2.7D, $\rho = -0.668$, $p < 0.0001$). As cortex glial globularity increases, shown by a lower AMI, astrocyte infiltration correspondingly increases, indicated by the strong negative correlation. Significant correlations ($p < 0.001$) among all groups are indicated by the yellow shaded region, which occurs throughout the dorsal- ventral axis with the exception of a small section in the middle of the VNC (52–64%, $p > 0.05$ from 55 to 60%).
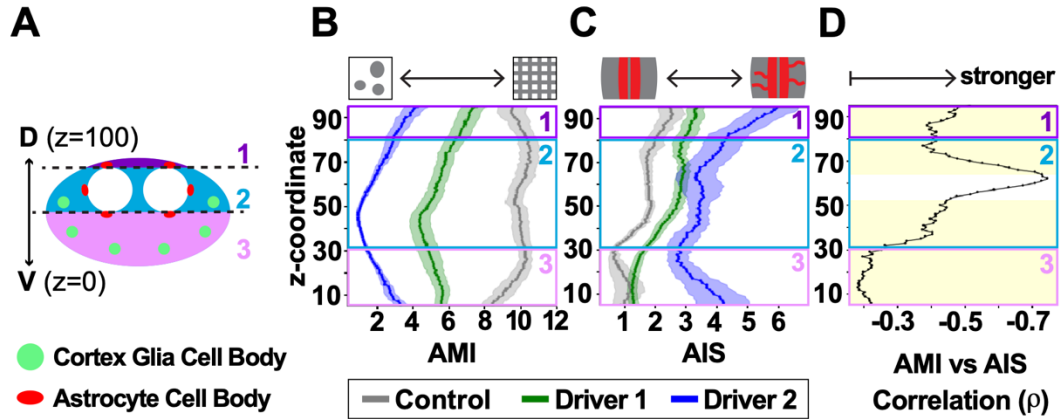
Fig. 2.7: Cortex glia morphology, aberrant astrocyte infiltration, and their relationship vary along the dorsal-ventral axis of the ventral nerve cord.
A) Cross-section depicting the larval VNC along dorsal-ventral axis, divided into three zones: above the dorsal astrocyte cell bodies (1, purple), along the neuropil (2, teal), and ventral to the neuropil (3, pink). The locations of astrocyte cell bodies are shown in red, and the stereotyped location of globular cortex glia in green. (B,C) A sliding window reveals differences along the dorsal-ventral axis in both CG AMI (B) and astrocyte AIS (C), with control (gray), driver 1 (green), and driver 2 (blue) depicted as mean ± SEM. (D) The relationship between AMI and AIS is shown along the dorsal-ventral axis as a black line indicating the Spearman's rank correlation coefficient (ρ) for any given coordinate. The yellow shaded area indicates regions where the correlation was significant between the two with $p < 0.001$.

2.5 Discussion

Glial tiling is a phenomenon that occurs throughout the animal kingdom [43], [48], [124], [125], [143], yet we still know relatively little about the formation, maintenance, and function of glial domains. While human astrocytes do still assemble into tiled domains, the extent of overlap of their processes is higher than in rodents [43], and astrocyte territories in species such as in ferrets can exhibit as much as 50% overlap in some astrocyte populations [45]. Interestingly, these tiling domains can also vary within the same species, such as in disease states like epilepsy [43] or even during normal aging [29]. Protoplasmic astrocytes in 5 month old adult mice show little to no overlap in their domains, yet the overlap increases in both cortical and hippocampal astrocytes nearly two- fold by 21 months of age [44]. Exactly what molecular cues regulate glial domain tiling and organization, and how and why these change in aging or disease is currently unclear.

We and others have shown that *Drosophila* present an exciting model to study the molecular underpinnings of glial tiling between either the same or disparate subtypes of glial cells. Rodent models that rely on genetic labeling of glial cells with Cre lines [144]–[146] often lack precise single cell genetic manipulation and differential control of adjacent cells. *Drosophila* provide genetic tools to easily target, label, and manipulate single cells within the same subtype (Fig. 2.1B–F), as well as multiple different glial subtypes

simultaneously (Fig. 2.1G–J), with a plethora of publicly available tools for genome-wide manipulation. Additionally, the domain organization of the *Drosophila* CNS allows for investigations of glial-glial tiling interactions that would be much more difficult in other organisms (Fig. 2.1A). Previous approaches have been applied to murine astrocytes to simplify the quantification of astrocyte tiling, such as using the volume of sparsely labeled astrocytes by Golgi impregnation, and taking into account the total astrocyte number in a given tissue area [44]. Interestingly, these authors found that in young mice, the overlap ratio of astrocytes was below 1, suggesting close interactions of other glial subtypes. Our previous findings that astrocytes react to cortex glial dysfunction by crossing the neuropil-cortex boundary [40] provided a basis for our current line of research. We wanted to build upon these findings to understand the extent of astrocyte reactivity when cortex glial morphology and tiling were disrupted; however, manual quantification of glial tiling is cumbersome, unfeasible on a large scale, and could miss more subtle differences in tiling variation. Here we have presented and validated an automated pipeline using free, open-source software to quantify both glial morphology and domain infiltration of adjacent glial subtypes in *Drosophila.* This tool allows for high-throughput quantification that, when combined with the power of genetics in this model system, will open the door for large scale, *in vivo* mechanistic studies of glial tiling.

The formation of globular cortex glia would be expected to leave neuronal cell bodies without any glial contact; however, the ability for glial cells to grow is quite impressive, and the surrounding healthy glia do not leave those neurons bare for long. Our previous work identified that upon the loss of Spz3 or αSNAP in cortex glia, thin astrocytic processes began to move into the cortex in late larval stages [40]. We have created and validated a pipeline to automatically quantify both cortex glia morphology (AMI) and aberrant astrocyte infiltration into the cortex (AIS) for over 3,300 images, with accuracy confirmed by comparison with manually obtained scores. Using this automated pipeline, we found that the extent of astrocyte infiltration strongly correlates with the extent of cortex glial disruption, but importantly, that this correlation remains regardless of the high degree of variation in both categories throughout the CNS. The observed variation could result from a number of different factors, including but not limited to glial heterogeneity, location and positioning of glial cells throughout the CNS, and driver strength. Glial heterogeneity is a current focus within the glial field to understand how different cells even within the same subtype (i.e., astrocytes)

differ in their molecular composition and functional roles. With the recent advancement of single-cell sequencing technologies [147], [148], cellular heterogeneity is becoming more widely understood beyond simple morphological differences such as fibrous or protoplasmic astrocytes. Different glial cells of the same subtype within a defined brain region can even exhibit molecular variation in signaling factors, receptors, transcription factors, and more [149]–[151], meaning that the same genetic perturbations in or near two adjacent cells could produce two very different reactions. While the extent of heterogeneity within each *Drosophila* glial subtype is thought to be less than that of mammalian glia, differences within the same subtype have been noted, such as the higher distribution of fatty acid binding protein (fabp) and lipid droplets in superficial cortex glia [152]. In the current study, we made use of two different driver systems: driver 1 was used to knock down Spz3 with the LexA system, resulting in a wider range of disrupted cortex glial morphology compared to the stronger driver 2, which uses the Gal4 system to knock down αSNAP. These differences in strength allowed us to investigate how astrocytes react to mild and more severe perturbations in glial tiling and boundary maintenance. Notably, the severity in AMI is more likely to be due to the strength of the driver rather than the molecule knocked down, as the Gal4-driven knockdown of Spz3 results in a similarly severe morphological disruption as Gal4-driven knockdown of αSNAP [40]; however, we cannot definitively rule out molecular differences, as the reduction of αSNAP could lead to restricted release of other secreted signaling factors. The differences in the degree of cortex glial disruption with driver 1, regardless of the underlying mechanism, allowed us to address the significant correlation between the extent of the globular morphology and aberrant astrocyte outgrowth, a result that was further supported with the stronger driver system.

The layout of the CNS is not homogenous throughout the dorsal-ventral axis. The neuropil is offset toward the dorsal side of the VNC (Fig. 2.1A'), with many astrocyte cell bodies distributed throughout this region. The ventral region of the VNC contains more cortex glia and neuronal cell bodies (zone 3, Fig. 2.7A), located farther from the neuropil where astrocyte processes reside. Therefore, if an astrocyte infiltration signal originates from cells within the ventral cortex, the signal could take longer to reach the astrocytes or never reach it at all. Alternatively, there could be a larger signal arising from the greater number of neuronal cell bodies within this region. Likewise, there is more space for astrocytes to grow in this direction. The

combination of these factors complicates the investigation of glial tiling, but the ability to automate quantification throughout the VNC allowed us to reveal differences in reactivity and correlation in spatial segregation along the dorsal-ventral axis that would have been difficult to identify via manual quantification alone, and to begin to parse out the cellular reactivity.

In addition to the dorsal alignment of the neuropil, the location of both astrocyte and cortex glial cell bodies is a potential source of AMI and AIS variation along the dorsal-ventral axis. While control *Drosophila* can have up to an average of 60– 80 cortex glial nuclei in the thoracic segments of the VNC, those with globular cortex glia average 6–10 nuclei per segment due to a failure to proliferate [40]. Moreover, these remaining globular cortex glial cells are located in stereotyped positions from animal to animal at the location where the cortex glial nuclei first align during development [40], [153]. This spacing leaves a greater distance between the neuropil and the ventral cortex glial cells (zone 3 in Fig. 2.7A) compared to those located in the more lateral position in the middle of the dorsal-ventral axis (zone 2 in Fig. 2.7A), and also allows for more variability if not all of the cortex glial cells are fully transformed from the mesh-like to globular morphology. Interestingly, the dorsal-most neurons of the VNC (zone 1, Fig. 2.7A) are encapsulated by cortex glia in the lateral portions, but a specialized type of ensheathing glia wrap the more medial neurons in this portion of the VNC [40], [129]. This could account for the greater variation in zone 1, along with the intriguing possibility that cortex glial dysfunction disrupts other adjacent glial subtypes beyond astrocytes. While it is clear that the aberrant infiltration is due to astrocytes extending processes into the cortex rather than a migration of the entire cell [40], astrocyte cell bodies do reside in the cortex along the interface of the cortex and neuropil [46]. In order to quantify only those processes that account for true aberrant infiltration, we identified characteristics of cell bodies that would allow for their automatic exclusion from the final infiltration count. However, slight remnants left behind from the sheer number of astrocyte cell bodies, could be artificially increasing infiltration scores in regions surrounding the neuropil (zones 1 and 2, Fig. 2.7A).

We found that AMI and AIS strongly correlate throughout the majority of the VNC, though our analysis revealed that cortex glial morphology, astrocyte infiltration, and their relationship varies along the dorsal-ventral axis. Moreover, there was still variation in AIS amongst different animals or regions even with strong disruption of cortex glial morphology. While the automated pipeline presented here is designed for

31

general use for anyone with access to simple imaging methods like confocal microscopy, one limitation is that glial domains are three- dimensional structures, and two-dimensional imaging can miss fine processes between the imaging intervals that could lead to an underestimation of glial territory and infiltration. Future development of a pipeline to work with three-dimensional imaging software and imaging techniques such as light sheet microscopy will further enhance these studies.

Identifying the molecular mechanisms that underly the development and maintenance of glial boundaries, and how and why glial cells respond to move out of their normal territories, as well as the functional consequences of doing so is paramount to furthering our understanding of the nervous system in health and disease. We now have a strong genetically tractable system to investigate these issues with an optimized tool for quantifying and revealing changes in glial tiling. This work raises a number of intriguing questions that we can use these tools to begin to answer: what are the molecular mechanisms involved in setting up and/or maintaining glial tiling? How do they change in aging or disease? Do glial tiling cues result only from glial-glial interactions or neuron-glial communication as well? Finally, if glia divert their cellular resources from their normal positions, such as astrocytes from the neuropil into the cortex, can they still maintain their normal functions? The combination of the automated pipeline provided here with the plethora of genetic tools available in *Drosophila* will allow us to begin to unlock the answers.

2.6 Supplementary Material
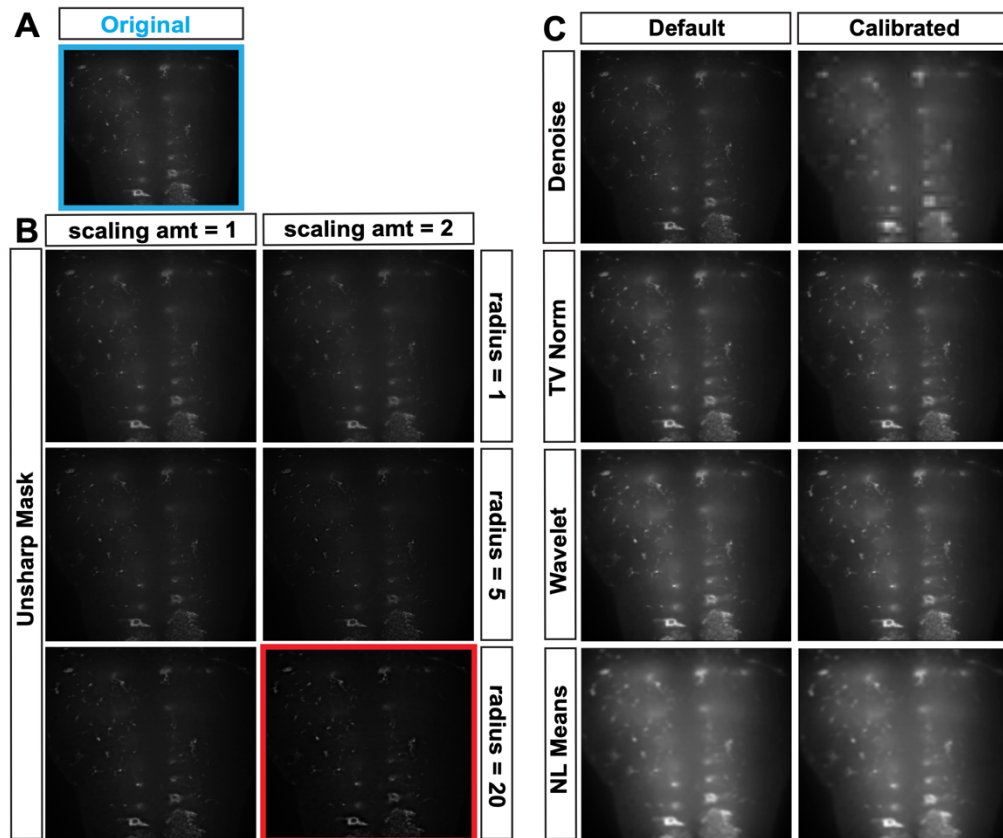
Fig. S2.1: Examples of denoising algorithms.

A) The original astrocyte image (blue outline) was denoised using different algorithms implement by scikit-image. B) Six panels resulting from denoising using an unsharp mask with different combinations of parameters, radius of 1, 5, or 20 and scaling amount (amt) 1 and 2. The red outline indicates the algorithm selected for denoising astrocyte images, as it produced the truest match of the original image. C) Eight panels resulting from denoising with denoise, non-local (NL), wavelet, and total-variation (TV) algorithms using two parameter combinations per algorithm: default and optimized using a J-invariant algorithm (calibrated).
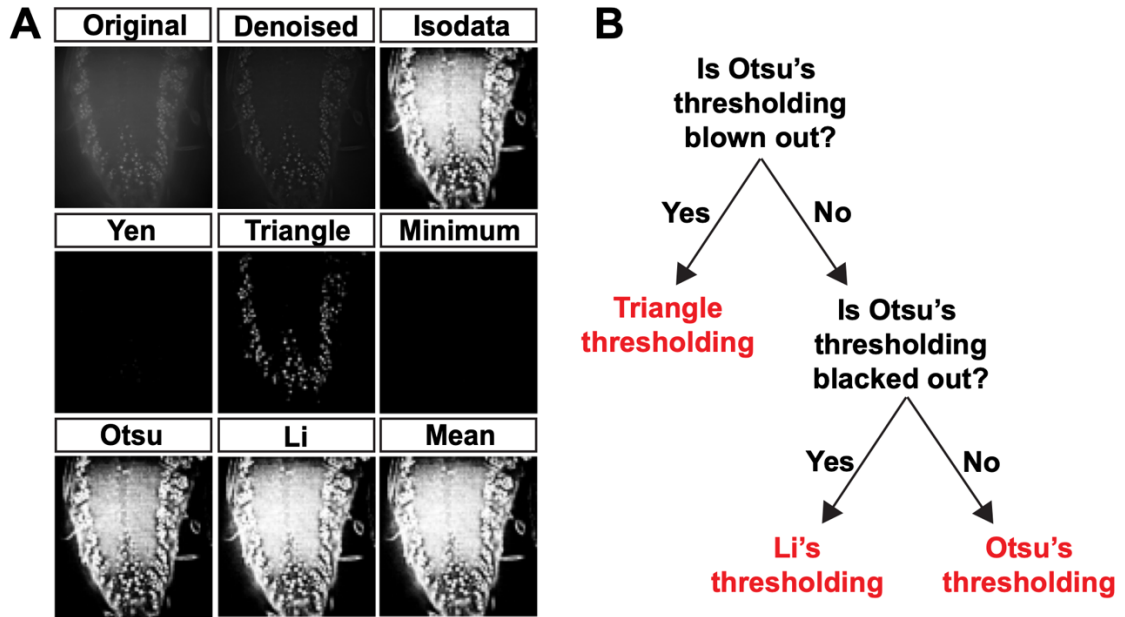
Fig. S2.2: Examples of binarization algorithms.
A) The original neuronal cell nuclear image was denoised and binarized by 7 global thresholding algorithms implemented by scikit-image. B) Decision tree used to determine the thresholding algorithm for each neuron image. Blown out images vastly overestimated the area covered by neurons, such as those produced by Isodata, Otsu, Li, and Mean algorithms in (A). Blacked out images are those that vastly underestimate the area covered by neurons, such as those produced by Minimum and Yen algorithms in (A). Similar decision trees were used to produce binary images for the cortex glia and astrocyte channels.
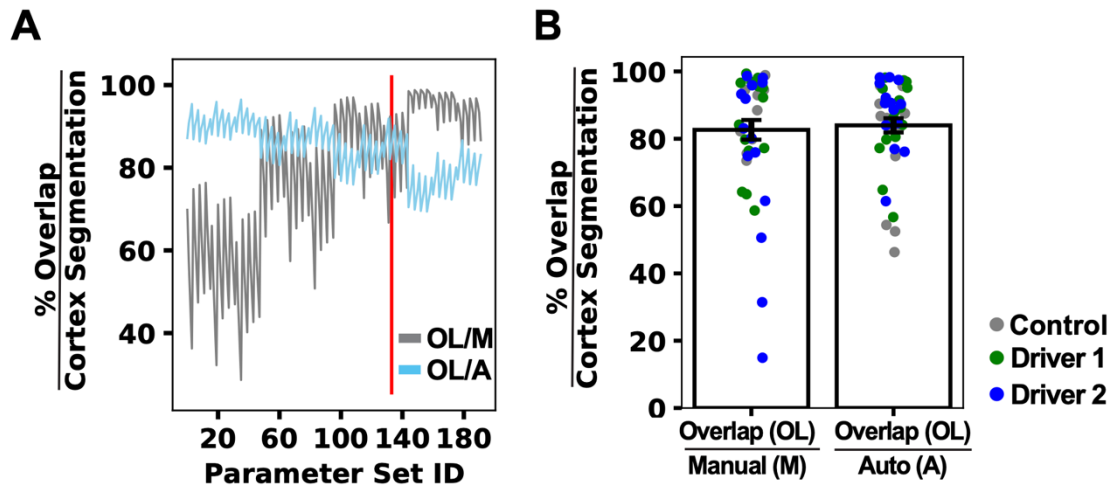
Fig. S2.3: Optimization and validation of automated cortex detection.
A) Automated cortex segmentation was produced for 42 images using 192 different parameter sets. The overlap (OL) between corresponding automated and manual segmentation was calculated. The average OL/manual ROI (OL/M) and OL/automated (OL/A) were used as performance metrics to select the best parameter combination (red line) for subsequent analyses. B) OL/Cortex Segmentation scores for the top-performing parameter combination for the 45 validation images (control: gray, driver 1: green, driver 2: blue).
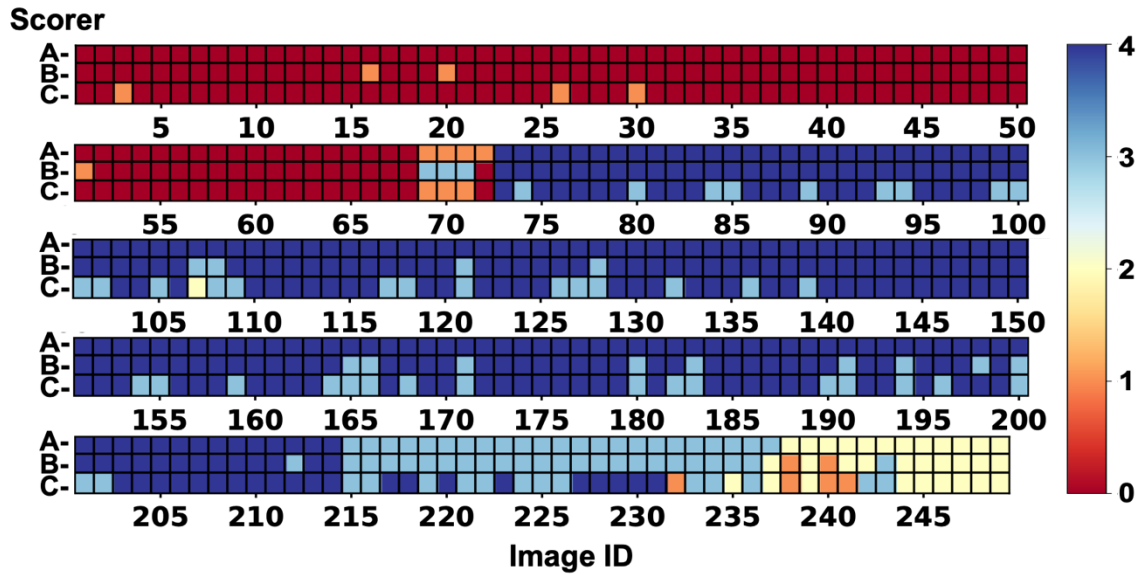
Fig. S2.4: Validation of the manual globularity score, and the ruling out of quantifier variability.

Heatmap illustrating the manual globularity score (MGS) for 249 images as determined by three blinded quantifiers. There is a high level of agreement between the scorers as indicated by the intraclass correlation (ICC(3,k)=0.983, p<0.001).

Chapter 3: Conclusion

3.1 Advantages of Image Analysis Pipeline

The greatest advantage of automating image analysis is that it can be used to maximize the size of the dataset that is analyzed. Larger datasets can reveal subtle patterns or patterns that apply to a larger portion of a system. These patterns can reveal information about the underlying mechanisms that control a system. Understanding how the nervous system functions is one of the primary goals of neuroscience research, and in the case of biomedical research has vast implications into how we can treat or even prevent disease. In the present study of glial-glial interactions, creating an automated pipeline enabled us to analyze a substantial portion of the *Drosophila* VNC, a cross-section equaling approximately one-third of the entire organ (Fig. 1A). The fly, like the mammalian, CNS is organized into different substructures, and we know that there are differences between the numerous structures – both in terms of which parts are present, e.g. which cell subtypes are located in different areas, and how these parts interact with each other [154]–[156]. Quantifying a large section of the VNC demonstrated how the cortex-glial-globularity-aberrant-astrocyte-infiltration relationship varies along the Z-axis, and by extension gives us information about how cortex glia and astrocytes might be interacting differently in different areas of the VNC. A thorough validation of the pipeline, in addition with results consistent with previous literature, namely that aberrant astrocyte infiltration increases in the presence of globular cortex glia [40], demonstrate that the results of the pipeline are accurate. Additionally, using open-source software to build the pipeline allows for transparency, customizability and wide access. By having full access to all code, users can inspect exactly which algorithms are used and how they were implemented, factors that can have a substantial impact on the final results, especially since many algorithms and models rely on certain assumptions. Full code-access also allows users to make any changes they deem necessary. Finally, the lack of a paywall allows researchers with even modest resources to use these tools, and promotes collaboration between groups, an essential principle for the advancement of science.

3.1 Shortcomings of Image Analysis Pipeline

Though the pipeline presented in this thesis was certainly useful in elucidating cortex-glial-astrocyte interactions, there are several drawbacks to this method. First, the pipeline works in 2D – it analyzes each slice separately and uses a smoothing algorithm to examine areas spanning several slices. The system the pipeline quantifies is a physical 3D system, however, and the most appropriate way to analyze it is in 3D. Additionally, though thresholding methods produced fairly accurate segmentations for the vast majority of the slices, it is possible to create more accurate segmentations with more sophisticated methods, namely using machine learning and deep learning. Producing highly precise segmentations is especially difficult while at the same time especially important in the case of astrocytes, since the parts of the cell in which we are most interested are very thin processes that extend into the cortex. These protrusions can be difficult to detect even by eye, and can be overestimated or even missed entirely by simple thresholding methods. Finally, this pipeline lacks generalizability. It is highly tailored to process images with the type and extent of noise, convolution, and signal attenuation present in the dataset analyzed in this study. As discussed previously, the quality of confocal images can vary due to many factors, including the type of staining that is done. Future studies in glial-glial interactions will include analyzing communication between cortex glia and glia other than astrocytes. Visualizing those other glial subtypes will involve using different antibodies which will result in images with differing levels of noise, convolution, and signal attenuation different from the ones in the current dataset. Adapting the pipeline to analyze those new images is possible, but is a difficult and tedious process.

3.2   Future Directions

As previously mentioned, future glial-glial interaction studies will include examining communication between additional glial subtypes. Improvements for the automated image analysis pipeline will include increasing its accuracy as well as adapting it to segment these additional cell types. The most significant improvement is moving from working in 2D to analyzing images in 3D. Pilot studies using machine and deep learning have shown we can obtain highly accurate segmentations for our dataset with both types of models, using Labkit to train a random forest model and deep learning to train U-NET. In our work, the trained random forest model has shown to be less generalizable than a trained U-NET. Hence, several different random forest segmentation models will need to be trained to segment the whole dataset, as

opposed to a single CNN per cell type. However, single random forest models do segment an entire Z-stack satisfactorily, and working in 3D would mean considering entire Z-stacks rather than single slices, which cuts the dataset by a factor of approximately 30. Even if segmentation of each Z-stack requires manual selection of the optimal segmentation algorithm from a small number of trained classifiers, the time investment required remains practical, as opposed to choosing the optimal algorithm for thousands of single slices. It is also possible that the selection process may be optimized exploiting characteristics such as a difference in texture, as was done in the original pipeline. Given the increased computing power, size of a labeled training dataset, and technical expertise necessary for training a CNN as compared to a random forest, the latter option will be explored first.

Imaging remains one of the most powerful tools in biomedical research, and continuous technological improvements allow for ever higher throughput experiments resulting in big and bigger data. Unfortunately, researchers often hit a bottleneck when attempting to analyze these large image-based datasets. Researchers and engineers are continuously developing new incredible image analysis tools. However, there is a need for even more tools and just as importantly for increased and continuous collaboration between image analysis experts and biomedical researchers to ensure that we can extract as much knowledge as possible from images, thus elucidating how the human body works in such as to enhance health and ameliorate disease.

Bibliography

[1]   P. Mazzarello, "A unifying concept: the history of cell theory," *Nat. Cell Biol.*, vol. 1, no. 1, Art. no. 1, May 1999, doi: 10.1038/8964.

[2]   N. de Jonge and F. M. Ross, "Electron microscopy of specimens in liquid," *Nat. Nanotechnol.*, vol. 6, no. 11, Art. no. 11, Nov. 2011, doi: 10.1038/nnano.2011.161.

[3]   M. Renz, "Fluorescence microscopy—A historical and technical perspective," *Cytometry A*, vol. 83, no. 9, pp. 767–779, 2013, doi: 10.1002/cyto.a.22295.

[4]   M. Cregger, A. J. Berger, and D. L. Rimm, "Immunohistochemistry and Quantitative Analysis of Protein Expression," *Arch. Pathol. Lab. Med.*, vol. 130, no. 7, pp. 1026–1030, Jul. 2006, doi: 10.5858/2006-130-1026-IAQAOP.

[5]   G. C. Giakos, M. Pastorino, F. Russo, S. Chowdhury, N. Shah, and W. Davros, "Noninvasive imaging for the new century," *IEEE Instrum. Meas. Mag.*, vol. 2, no. 2, pp. 32–35, Jun. 1999, doi: 10.1109/5289.765967.

[6]   V. Chan and A. Perlas, "Basics of Ultrasound Imaging," in *Atlas of Ultrasound-Guided Procedures in Interventional Pain Management*, S. N. Narouze, Ed., New York, NY: Springer, 2011, pp. 13–19. doi: 10.1007/978-1-4419-1681-5_2.

[7]   N. K. Logothetis, "What we can do and what we cannot do with fMRI," *Nature*, vol. 453, no. 7197, Art. no. 7197, Jun. 2008, doi: 10.1038/nature06976.

[8]   C. S. von Bartheld, J. Bahney, and S. Herculano-Houzel, "The search for true numbers of neurons and glial cells in the human brain: A review of 150 years of cell counting," *J. Comp. Neurol.*, vol. 524, no. 18, pp. 3865–3895, 2016, doi: 10.1002/cne.24040.

[9]   B. J. He, G. L. Shulman, A. Z. Snyder, and M. Corbetta, "The role of impaired neuronal communication in neurological disorders," *Curr. Opin. Neurol.*, vol. 20, no. 6, p. 655, Dec. 2007, doi: 10.1097/WCO.0b013e3282f1c720.

[10]   S. K. Schmitz *et al.*, "Automated analysis of neuronal morphology, synapse number and synaptic recruitment," *J. Neurosci. Methods*, vol. 195, no. 2, pp. 185–193, Feb. 2011, doi: 10.1016/j.jneumeth.2010.12.011.

[11]   A. H. de Haas, H. R. J. van Weering, E. K. de Jong, H. W. G. M. Boddeke, and K. P. H. Biber, "Neuronal Chemokines: Versatile Messengers In Central Nervous System Cell Interaction," *Mol. Neurobiol.*, vol. 36, no. 2, pp. 137–151, Oct. 2007, doi: 10.1007/s12035-007-0036-8.

[12]   I. C. Clark *et al.*, "Barcoded viral tracing of single-cell interactions in central nervous system inflammation," *Science*, vol. 372, no. 6540, p. eabf1230, Apr. 2021, doi: 10.1126/science.abf1230.

[13]   A. Schnatz, C. Müller, A. Brahmer, and E. Krämer-Albers, "Extracellular Vesicles in neural cell interaction and CNS homeostasis," *FASEB BioAdvances*, vol. 3, no. 8, pp. 577–592, May 2021, doi: 10.1096/fba.2021-00035.

[14]   B. B. Lake *et al.*, "Neuronal subtypes and diversity revealed by single-nucleus RNA sequencing of the human brain," *Science*, vol. 352, no. 6293, pp. 1586–1590, Jun. 2016, doi: 10.1126/science.aaf1204.

[15]   F. Marmigère and P. Ernfors, "Specification and connectivity of neuronal subtypes in the sensory lineage," *Nat. Rev. Neurosci.*, vol. 8, no. 2, Art. no. 2, Feb. 2007, doi: 10.1038/nrn2057.

[16]   B. J. Molyneaux, P. Arlotta, J. R. L. Menezes, and J. D. Macklis, "Neuronal subtype specification in the cerebral cortex," *Nat. Rev. Neurosci.*, vol. 8, no. 6, Art. no. 6, Jun. 2007, doi: 10.1038/nrn2151.

[17]   M. V. Sofroniew, "Astrocyte Reactivity: Subtypes, States, and Functions in CNS Innate Immunity," *Trends Immunol.*, vol. 41, no. 9, pp. 758–770, Sep. 2020, doi: 10.1016/j.it.2020.07.004.

[18]   L. Schirmer, D. P. Schafer, T. Bartels, D. H. Rowitch, and P. A. Calabresi, "Diversity and Function of Glial Cell Types in Multiple Sclerosis," *Trends Immunol.*, vol. 42, no. 3, pp. 228–247, Mar. 2021, doi: 10.1016/j.it.2021.01.005.

[19]   L. Pinto *et al.*, "Prospective isolation of functionally distinct radial glial subtypes—Lineage and transcriptome analysis," *Mol. Cell. Neurosci.*, vol. 38, no. 1, pp. 15–42, May 2008, doi: 10.1016/j.mcn.2008.01.012.

[20]   N. J. Allen and B. A. Barres, "Glia — more than just brain glue," *Nature*, vol. 457, no. 7230, Art. no. 7230, Feb. 2009, doi: 10.1038/457675a.

[21] W. s. t. Griffin *et al.*, "Glial-Neuronal Interactions in Alzheimer's Disease: The Potential Role of a 'Cytokine Cycle' in Disease Progression," *Brain Pathol.*, vol. 8, no. 1, pp. 65–72, 1998, doi: 10.1111/j.1750-3639.1998.tb00136.x.

[22] E. Vecino, F. D. Rodriguez, N. Ruzafa, X. Pereiro, and S. C. Sharma, "Glia–neuron interactions in the mammalian retina," *Prog. Retin. Eye Res.*, vol. 51, pp. 1–40, Mar. 2016, doi: 10.1016/j.preteyeres.2015.06.003.

[23] S. Shaham, "Glia–Neuron Interactions in Nervous System Function and Development," in *Current Topics in Developmental Biology*, in Neural Development, vol. 69. Academic Press, 2005, pp. 39–66. doi: 10.1016/S0070-2153(05)69003-5.

[24] J. M. Schwarz and S. D. Bilbo, "Sex, glia, and development: Interactions in health and disease," *Horm. Behav.*, vol. 62, no. 3, pp. 243–253, Aug. 2012, doi: 10.1016/j.yhbeh.2012.02.018.

[25] T. Awasaki, S.-L. Lai, K. Ito, and T. Lee, "Organization and postembryonic development of glial cells in the adult central brain of Drosophila," *J. Neurosci. Off. J. Soc. Neurosci.*, vol. 28, no. 51, pp. 13742–13753, Dec. 2008, doi: 10.1523/JNEUROSCI.4844-08.2008.

[26] M. G. Andrews, L. Subramanian, and A. R. Kriegstein, "mTOR signaling regulates the morphology and migration of outer radial glia in developing human cortex," *eLife*, vol. 9, p. e58737, Sep. 2020, doi: 10.7554/eLife.58737.

[27] N. J. Allen, "Role of glia in developmental synapse formation," *Curr. Opin. Neurobiol.*, vol. 23, no. 6, pp. 1027–1033, Dec. 2013, doi: 10.1016/j.conb.2013.06.004.

[28] D. Dahl, "The radial glia of Müller in the rat retina and their response to injury. An immunofluorescence study with antibodies to the glial fibrillary acidic (GFA) protein," *Exp. Eye Res.*, vol. 28, no. 1, pp. 63–69, Jan. 1979, doi: 10.1016/0014-4835(79)90106-4.

[29] S. A. Back and P. A. Rosenberg, "Pathophysiology of glia in perinatal white matter injury," *Glia*, vol. 62, no. 11, pp. 1790–1815, 2014, doi: 10.1002/glia.22658.

[30] M. E. Hatten, R. K. H. Liem, M. L. Shelanski, and C. A. Mason, "Astroglia in CNS injury," *Glia*, vol. 4, no. 2, pp. 233–243, 1991, doi: 10.1002/glia.440040215.

[31] M. Svensson, P. Eriksson, J. K. E. Persson, C. Molander, J. Arvidsson, and H. Aldskogius, "The response of central glia to peripheral nerve injury," *Brain Res. Bull.*, vol. 30, no. 3, pp. 499–506, Jan. 1993, doi: 10.1016/0361-9230(93)90284-I.

[32] F. Zeidán-Chuliá, A. B. Salmina, N. A. Malinovskaya, M. Noda, A. Verkhratsky, and J. C. F. Moreira, "The glial perspective of autism spectrum disorders," *Neurosci. Biobehav. Rev.*, vol. 38, pp. 160–172, Jan. 2014, doi: 10.1016/j.neubiorev.2013.11.008.

[33] X. Jin *et al.*, "In vivo Perturb-Seq reveals neuronal and glial abnormalities associated with autism risk genes," *Science*, vol. 370, no. 6520, p. eaaz6063, Nov. 2020, doi: 10.1126/science.aaz6063.

[34] L. M. Healy, J. A. Stratton, T. Kuhlmann, and J. Antel, "The role of glial cells in multiple sclerosis disease progression," *Nat. Rev. Neurol.*, vol. 18, no. 4, Art. no. 4, Apr. 2022, doi: 10.1038/s41582-022-00624-x.

[35] M. Orre *et al.*, "Isolation of glia from Alzheimer's mice reveals inflammation and dysfunction," *Neurobiol. Aging*, vol. 35, no. 12, pp. 2746–2760, Dec. 2014, doi: 10.1016/j.neurobiolaging.2014.06.004.

[36] N. Koning, D. F. Swaab, R. M. Hoek, and I. Huitinga, "Distribution of the Immune Inhibitory Molecules CD200 and CD200R in the Normal Central Nervous System and Multiple Sclerosis Lesions Suggests Neuron-Glia and Glia-Glia Interactions," *J. Neuropathol. Exp. Neurol.*, vol. 68, no. 2, pp. 159–167, Feb. 2009, doi: 10.1097/NEN.0b013e3181964113.

[37] R. Bernard *et al.*, "Altered expression of glutamate signaling, growth factor, and glia genes in the locus coeruleus of patients with major depression," *Mol. Psychiatry*, vol. 16, no. 6, Art. no. 6, Jun. 2011, doi: 10.1038/mp.2010.44.

[38] A. G. Dietz, S. A. Goldman, and M. Nedergaard, "Glial cells in schizophrenia: a unified hypothesis," *Lancet Psychiatry*, vol. 7, no. 3, pp. 272–281, Mar. 2020, doi: 10.1016/S2215-0366(19)30302-5.

[39] C. Hercher, V. Chopra, and C. L. Beasley, "Evidence for morphological alterations in prefrontal white matter glia in schizophrenia and bipolar disorder," *J. Psychiatry Neurosci.*, vol. 39, no. 6, pp. 376–385, Nov. 2014, doi: 10.1503/jpn.130277.

[40] J. C. Coutinho-Budd, A. E. Sheehan, and M. R. Freeman, "The secreted neurotrophin Spätzle 3 promotes glial morphogenesis and supports neuronal survival and function," *Genes Dev.*, vol. 31, no. 20, pp. 2023–2038, Oct. 2017, doi: 10.1101/gad.305888.117.

[41] H. Aldskogius and E. N. Kozlova, "Central neuron–glial and glial–glial interactions following axon injury," *Prog. Neurobiol.*, vol. 55, no. 1, pp. 1–26, May 1998, doi: 10.1016/S0301-0082(97)00093-2.

[42] E. A. Bushong, M. E. Martone, Y. Z. Jones, and M. H. Ellisman, "Protoplasmic astrocytes in CA1 stratum radiatum occupy separate anatomical domains," *J. Neurosci. Off. J. Soc. Neurosci.*, vol. 22, no. 1, pp. 183–192, Jan. 2002, doi: 10.1523/JNEUROSCI.22-01-00183.2002.

[43] N. A. Oberheim *et al.*, "Uniquely Hominid Features of Adult Human Astrocytes," *J. Neurosci.*, vol. 29, no. 10, pp. 3276–3287, Mar. 2009, doi: 10.1523/JNEUROSCI.4707-08.2009.

[44] A. Grosche *et al.*, "Versatile and Simple Approach to Determine Astrocyte Territories in Mouse Neocortex and Hippocampus," *PLoS ONE*, vol. 8, no. 7, p. e69143, Jul. 2013, doi: 10.1371/journal.pone.0069143.

[45] M. López-Hidalgo, W. B. Hoover, and J. Schummers, "Spatial organization of astrocytes in ferret visual cortex," *J. Comp. Neurol.*, vol. 524, no. 17, pp. 3561–3576, 2016, doi: 10.1002/cne.24015.

[46] A. K. Muthukumar, T. Stork, and M. R. Freeman, "Activity-dependent regulation of astrocyte GAT levels during synaptogenesis," *Nat. Neurosci.*, vol. 17, no. 10, Art. no. 10, Oct. 2014, doi: 10.1038/nn.3791.

[47] J. Chen, K. E. Poskanzer, M. R. Freeman, and K. R. Monk, "Live-imaging of astrocyte morphogenesis and function in zebrafish neural circuits," *Nat. Neurosci.*, vol. 23, no. 10, pp. 1297–1306, Oct. 2020, doi: 10.1038/s41593-020-0703-x.

[48] H. Kettenmann, F. Kirchhoff, and A. Verkhratsky, "Microglia: New Roles for the Synaptic Stripper," *Neuron*, vol. 77, no. 1, pp. 10–18, Jan. 2013, doi: 10.1016/j.neuron.2012.12.023.

[49] B. Katz and B. Minke, "Drosophila photoreceptors and signaling mechanisms," *Front. Cell. Neurosci.*, vol. 3, 2009, Accessed: Jul. 21, 2023. [Online]. Available: https://www.frontiersin.org/articles/10.3389/neuro.03.002.2009

[50] A. B. Ziegler, M. Berthelot-Grosjean, and Y. Grosjean, "The smell of love in Drosophila," *Front. Physiol.*, vol. 4, 2013, Accessed: Jul. 21, 2023. [Online]. Available: https://www.frontiersin.org/articles/10.3389/fphys.2013.00072

[51] E. S. Levitan, F. Lanni, and D. Shakiryanova, "In vivo imaging of vesicle motion and release at the Drosophila neuromuscular junction," *Nat. Protoc.*, vol. 2, no. 5, Art. no. 5, May 2007, doi: 10.1038/nprot.2007.142.

[52] C. Zhou, Y. Rao, and Y. Rao, "A subset of octopaminergic neurons are important for Drosophila aggression," *Nat. Neurosci.*, vol. 11, no. 9, Art. no. 9, Sep. 2008, doi: 10.1038/nn.2164.

[53] H. J. Pavlou and S. F. Goodwin, "Courtship behavior in Drosophila melanogaster: towards a 'courtship connectome,'" *Curr. Opin. Neurobiol.*, vol. 23, no. 1, pp. 76–83, Feb. 2013, doi: 10.1016/j.conb.2012.09.002.

[54] T. Suzuki, M. Kaido, R. Takayama, and M. Sato, "A temporal mechanism that produces neuronal diversity in the Drosophila visual center," *Dev. Biol.*, vol. 380, no. 1, pp. 12–24, Aug. 2013, doi: 10.1016/j.ydbio.2013.05.002.

[55] S. Lin and T. Lee, "Generating neuronal diversity in the Drosophila central nervous system," *Dev. Dyn.*, vol. 241, no. 1, pp. 57–68, 2012, doi: 10.1002/dvdy.22739.

[56] K. Yildirim, J. Petri, R. Kottmeier, and C. Klämbt, "Drosophila glia: Few cell types and many conserved functions," *Glia*, vol. 67, no. 1, pp. 5–26, Jan. 2019, doi: 10.1002/glia.23459.

[57] H. J. Bellen, C. Tong, and H. Tsuda, "100 years of Drosophila research and its impact on vertebrate neuroscience: a history lesson for the future," *Nat. Rev. Neurosci.*, vol. 11, no. 7, pp. 514–522, Jul. 2010, doi: 10.1038/nrn2839.

[58] A. del Valle Rodríguez, D. Didiano, and C. Desplan, "Power tools for gene expression and clonal analysis in Drosophila," *Nat. Methods*, vol. 9, no. 1, Art. no. 1, Jan. 2012, doi: 10.1038/nmeth.1800.

[59] A. Nwaneshiudu, C. Kuschal, F. H. Sakamoto, R. R. Anderson, K. Schwarzenberger, and R. C. Young, "Introduction to Confocal Microscopy," *J. Invest. Dermatol.*, vol. 132, no. 12, pp. 1–5, Dec. 2012, doi: 10.1038/jid.2012.429.

[60] K. A. Leithner, "Basics of quantitative image analysis," *Adv. Mater. Process. U. S.*, vol. 144:5, Nov. 1993, Accessed: Jul. 21, 2023. [Online]. Available: https://www.osti.gov/biblio/5522987

[61] S. Nazlibilek, D. Karacor, T. Ercan, M. H. Sazli, O. Kalender, and Y. Ege, "Automatic segmentation, counting, size determination and classification of white blood cells," *Measurement*, vol. 55, pp. 58–65, Sep. 2014, doi: 10.1016/j.measurement.2014.04.008.

[62] S.-J. Lim, Y.-Y. Jeong, and Y.-S. Ho, "Automatic liver segmentation for volume measurement in CT Images," *J. Vis. Commun. Image Represent.*, vol. 17, no. 4, pp. 860–875, Aug. 2006, doi: 10.1016/j.jvcir.2005.07.001.

[63] D. T. Chard, G. J. M. Parker, C. M. B. Griffin, A. J. Thompson, and D. H. Miller, "The reproducibility and sensitivity of brain tissue volume measurements derived from an SPM-based segmentation methodology," *J. Magn. Reson. Imaging*, vol. 15, no. 3, pp. 259–267, 2002, doi: 10.1002/jmri.10064.

[64] S. Al-Fahdawi *et al.*, "A fully automated cell segmentation and morphometric parameter system for quantifying corneal endothelial cell morphology," *Comput. Methods Programs Biomed.*, vol. 160, pp. 11–23, Jul. 2018, doi: 10.1016/j.cmpb.2018.03.015.

[65] J. Prinyakupt and C. Pluempitiwiriyawej, "Segmentation of white blood cells and comparison of cell morphology by linear and naïve Bayes classifiers," *Biomed. Eng. OnLine*, vol. 14, no. 1, p. 63, Jun. 2015, doi: 10.1186/s12938-015-0037-1.

[66] V. Ulman *et al.*, "An objective comparison of cell-tracking algorithms," *Nat. Methods*, vol. 14, no. 12, pp. 1141–1152, Dec. 2017, doi: 10.1038/nmeth.4473.

[67] K. Benkrid, D. Crookes, and A. Benkrid, "Design and FPGA implementation of a perimeter estimator," *Proc. Ir. Mach. Vis. Image Process. Conf.*, pp. 51–57, Jan. 2000.

[68] S. van der Walt *et al.*, "scikit-image: image processing in Python," *PeerJ*, vol. 2, p. e453, Jun. 2014, doi: 10.7717/peerj.453.

[69] C. Kervrann and A. Trubuil, "An adaptive window approach for Poisson noise reduction and structure preserving in confocal microscopy," in *2004 2nd IEEE International Symposium on Biomedical Imaging: Nano to Macro (IEEE Cat No. 04EX821)*, Apr. 2004, pp. 788-791 Vol. 1. doi: 10.1109/ISBI.2004.1398656.

[70] M. Čapek, J. Janáček, and L. Kubínová, "Methods for compensation of the light attenuation with depth of images captured by a confocal microscope," *Microsc. Res. Tech.*, vol. 69, no. 8, pp. 624–635, 2006, doi: 10.1002/jemt.20330.

[71] G. M. P. Van Kempen, L. J. Van Vliet, P. J. Verveer, and H. T. M. Van Der Voort, "A quantitative comparison of image restoration methods for confocal microscopy," *J. Microsc.*, vol. 185, no. 3, pp. 354–365, 1997, doi: 10.1046/j.1365-2818.1997.d01-629.x.

[72] M. Sezgin and B. Sankur, "Survey over image thresholding techniques and quantitative performance evaluation," *J. Electron. Imaging*, vol. 13, no. 1, pp. 146–165, Jan. 2004, doi: 10.1117/1.1631315.

[73] G. James, D. Witten, T. Hastie, and R. Tibshirani, Eds., *An introduction to statistical learning: with applications in R*. in Springer texts in statistics, no. 103. New York: Springer, 2013.

[74] S. Berg *et al.*, "ilastik: interactive machine learning for (bio)image analysis," *Nat. Methods*, vol. 16, no. 12, Art. no. 12, Dec. 2019, doi: 10.1038/s41592-019-0582-9.

[75] M. Arzt *et al.*, "LABKIT: Labeling and Segmentation Toolkit for Big Image Data," *Front. Comput. Sci.*, vol. 4, 2022, Accessed: Jul. 21, 2023. [Online]. Available: https://www.frontiersin.org/articles/10.3389/fcomp.2022.777728

[76] D. Shen, G. Wu, and H.-I. Suk, "Deep Learning in Medical Image Analysis," *Annu. Rev. Biomed. Eng.*, vol. 19, no. 1, pp. 221–248, 2017, doi: 10.1146/annurev-bioeng-071516-044442.

[77] G.-M. Makris *et al.*, "Image analysis and multi-layer perceptron artificial neural networks for the discrimination between benign and malignant endometrial lesions," *Diagn. Cytopathol.*, vol. 45, no. 3, pp. 202–211, 2017, doi: 10.1002/dc.23649.

[78] A. S. Heinsfeld, A. R. Franco, R. C. Craddock, A. Buchweitz, and F. Meneguzzi, "Identification of autism spectrum disorder using deep learning and the ABIDE dataset," *NeuroImage Clin.*, vol. 17, pp. 16–23, Jan. 2018, doi: 10.1016/j.nicl.2017.08.017.

[79] M. Y. Ahmad, A. Mohamed, Y. A. Mohd Yusof, and S. A. Md. Ali, "Colorectal cancer image classification using image pre-processing and multilayer Perceptron," in *2012 International Conference on Computer & Information Science (ICCIS)*, Jun. 2012, pp. 275–280. doi: 10.1109/ICCISci.2012.6297253.

[80] L. K. Scheffer *et al.*, "A connectome and analysis of the adult Drosophila central brain," *eLife*, vol. 9, p. e57443, Sep. 2020, doi: 10.7554/eLife.57443.

[81] M. Xu, D. P. Papageorgiou, S. Z. Abidi, M. Dao, H. Zhao, and G. E. Karniadakis, "A deep convolutional neural network for classification of red blood cells in sickle cell anemia," *PLOS Comput. Biol.*, vol. 13, no. 10, p. e1005746, Oct. 2017, doi: 10.1371/journal.pcbi.1005746.

[82] S. K. Sadanandan, P. Ranefall, S. Le Guyader, and C. Wählby, "Automated Training of Deep Convolutional Neural Networks for Cell Segmentation," *Sci. Rep.*, vol. 7, no. 1, Art. no. 1, Aug. 2017, doi: 10.1038/s41598-017-07599-6.

[83] A. Lagree *et al.*, "A review and comparison of breast tumor cell nuclei segmentation performances using deep convolutional neural networks," *Sci. Rep.*, vol. 11, no. 1, Art. no. 1, Apr. 2021, doi: 10.1038/s41598-021-87496-1.

[84] T. M. Quan, D. G. C. Hildebrand, and W.-K. Jeong, "FusionNet: A Deep Fully Residual Convolutional Neural Network for Image Segmentation in Connectomics," *Front. Comput. Sci.*, vol. 3, 2021, Accessed: Jul. 22, 2023. [Online]. Available: https://www.frontiersin.org/articles/10.3389/fcomp.2021.613981

[85] T. Wollmann, M. Gunkel, I. Chung, H. Erfle, K. Rippe, and K. Rohr, "GRUU-Net: Integrated convolutional and gated recurrent neural network for cell segmentation," *Med. Image Anal.*, vol. 56, pp. 68–79, Aug. 2019, doi: 10.1016/j.media.2019.04.011.

[86] O. Ronneberger, P. Fischer, and T. Brox, "U-Net: Convolutional Networks for Biomedical Image Segmentation." arXiv, May 18, 2015. doi: 10.48550/arXiv.1505.04597.

[87] A. Abraham *et al.*, "Machine learning for neuroimaging with scikit-learn," *Front. Neuroinformatics*, vol. 8, 2014, Accessed: Jul. 22, 2023. [Online]. Available: https://www.frontiersin.org/articles/10.3389/fninf.2014.00014

[88] S. Beagum, N. Dey, A. S. Ashour, D. Sifaki-Pistolla, and V. E. Balas, "Nonparametric de-noising filter optimization using structure-based microscopic image classification," *Microsc. Res. Tech.*, vol. 80, no. 4, pp. 419–429, 2017, doi: 10.1002/jemt.22811.

[89] L. Shen, J. Lin, S. Wu, and S. Yu, "HEp-2 image classification using intensity order pooling based features and bag of words," *Pattern Recognit.*, vol. 47, no. 7, pp. 2419–2427, Jul. 2014, doi: 10.1016/j.patcog.2013.09.020.

[90] Y. Xu, J.-Y. Zhu, E. Chang, and Z. Tu, "Multiple clustered instance learning for histopathology cancer image classification, segmentation and clustering," in *2012 IEEE Conference on Computer Vision and Pattern Recognition*, Jun. 2012, pp. 964–971. doi: 10.1109/CVPR.2012.6247772.

[91] A. Suhre, F. Keskin, T. Ersahin, R. Cetin-Atalay, R. Ansari, and A. E. Cetin, "A multiplication-free framework for signal processing and applications in biomedical image analysis," in *2013 IEEE International Conference on Acoustics, Speech and Signal Processing*, May 2013, pp. 1123–1127. doi: 10.1109/ICASSP.2013.6637825.

[92] M. S. Sharif, R. Qahwaji, S. Ipson, and A. Brahma, "Medical image classification based on artificial intelligence approaches: A practical study on normal and abnormal confocal corneal images," *Appl. Soft Comput.*, vol. 36, pp. 269–282, Nov. 2015, doi: 10.1016/j.asoc.2015.07.019.

[93] C.-K. Shie, C.-H. Chuang, C.-N. Chou, M.-H. Wu, and E. Y. Chang, "Transfer representation learning for medical image analysis," in *2015 37th Annual International Conference of the IEEE Engineering in Medicine and Biology Society (EMBC)*, Aug. 2015, pp. 711–714. doi: 10.1109/EMBC.2015.7318461.

[94] S. Sladojevic, M. Arsenovic, A. Anderla, D. Culibrk, and D. Stefanovic, "Deep Neural Networks Based Recognition of Plant Diseases by Leaf Image Classification," *Comput. Intell. Neurosci.*, vol. 2016, p. e3289801, Jun. 2016, doi: 10.1155/2016/3289801.

[95] B. Kieffer, M. Babaie, S. Kalra, and H. R. Tizhoosh, "Convolutional neural networks for histopathology image classification: Training vs. Using pre-trained networks," in *2017 Seventh International Conference on Image Processing Theory, Tools and Applications (IPTA)*, Nov. 2017, pp. 1–6. doi: 10.1109/IPTA.2017.8310149.

[96] B. Q. Huynh, H. Li, and M. L. Giger, "Digital mammographic tumor classification using transfer learning from deep convolutional neural networks," *J. Med. Imaging*, vol. 3, no. 3, p. 034501, Aug. 2016, doi: 10.1117/1.JMI.3.3.034501.

[97] M. Talo, U. B. Baloglu, Ö. Yıldırım, and U. Rajendra Acharya, "Application of deep transfer learning for automated brain abnormality classification using MR images," *Cogn. Syst. Res.*, vol. 54, pp. 176–188, May 2019, doi: 10.1016/j.cogsys.2018.12.007.

[98] M. Sandler, A. Howard, M. Zhu, A. Zhmoginov, and L.-C. Chen, "MobileNetV2: Inverted Residuals and Linear Bottlenecks." arXiv, Mar. 21, 2019. doi: 10.48550/arXiv.1801.04381.

[99] G. Gunner *et al.*, "Sensory lesioning induces microglial synapse elimination via ADAM10 and fractalkine signaling," *Nat. Neurosci.*, vol. 22, no. 7, pp. 1075–1088, Jul. 2019, doi: 10.1038/s41593-019-0419-y.

[100] S. R. Spindler, I. Ortiz, S. Fung, S. Takashima, and V. Hartenstein, "Drosophila cortex and neuropile glia influence secondary axon tract growth, pathfinding, and fasciculation in the developing larval brain," *Dev. Biol.*, vol. 334, no. 2, pp. 355–368, Oct. 2009, doi: 10.1016/j.ydbio.2009.07.035.

[101] D. P. Schafer *et al.*, "Microglia Sculpt Postnatal Neural Circuits in an Activity and Complement-Dependent Manner," *Neuron*, vol. 74, no. 4, pp. 691–705, May 2012, doi: 10.1016/j.neuron.2012.03.026.

[102] O. E. Tasdemir-Yilmaz and M. R. Freeman, "Astrocytes engage unique molecular programs to engulf pruned neuronal debris from distinct subsets of neurons," *Genes Dev.*, vol. 28, no. 1, pp. 20–33, Jan. 2014, doi: 10.1101/gad.229518.113.

[103] S. Werneburg *et al.*, "Targeted Complement Inhibition at Synapses Prevents Microglial Synaptic Engulfment and Synapse Loss in Demyelinating Disease," *Immunity*, vol. 52, no. 1, pp. 167-182.e7, Jan. 2020, doi: 10.1016/j.immuni.2019.12.004.

[104] J. M. MacDonald, M. G. Beach, E. Porpiglia, A. E. Sheehan, R. J. Watts, and M. R. Freeman, "The Drosophila Cell Corpse Engulfment Receptor Draper Mediates Glial Clearance of Severed Axons," *Neuron*, vol. 50, no. 6, pp. 869–881, Jun. 2006, doi: 10.1016/j.neuron.2006.04.028.

[105] S. Hong *et al.*, "Complement and microglia mediate early synapse loss in Alzheimer mouse models," *Science*, vol. 352, no. 6286, pp. 712–716, May 2016, doi: 10.1126/science.aad8373.

[106] C. N. McLaughlin, J. J. Perry-Richardson, J. C. Coutinho-Budd, and H. T. Broihier, "Dying Neurons Utilize Innate Immune Signaling to Prime Glia for Phagocytosis during Development," *Dev. Cell*, vol. 48, no. 4, pp. 506-522.e6, Feb. 2019, doi: 10.1016/j.devcel.2018.12.019.

[107] F. Li *et al.*, "Glial Metabolic Rewiring Promotes Axon Regeneration and Functional Recovery in the Central Nervous System," *Cell Metab.*, vol. 32, no. 5, pp. 767-785.e7, Nov. 2020, doi: 10.1016/j.cmet.2020.08.015.

[108] A. Volkenhoff, A. Weiler, M. Letzel, M. Stehling, C. Klämbt, and S. Schirmeier, "Glial Glycolysis Is Essential for Neuronal Survival in Drosophila," *Cell Metab.*, vol. 22, no. 3, pp. 437–447, Sep. 2015, doi: 10.1016/j.cmet.2015.07.006.

[109] V. M. Fernandes, Z. Chen, A. M. Rossi, J. Zipfel, and C. Desplan, "Glia relay differentiation cues to coordinate neuronal development in Drosophila," *Science*, vol. 357, no. 6354, pp. 886–891, Sep. 2017, doi: 10.1126/science.aan3174.

[110] M. S. Ioannou *et al.*, "Neuron-Astrocyte Metabolic Coupling Protects against Activity-Induced Fatty Acid Toxicity," *Cell*, vol. 177, no. 6, pp. 1522-1535.e14, May 2019, doi: 10.1016/j.cell.2019.04.001.

[111] K.-A. Nave and H. B. Werner, "Ensheathment and Myelination of Axons: Evolution of Glial Functions," *Annu. Rev. Neurosci.*, vol. 44, no. 1, pp. 197–219, 2021, doi: 10.1146/annurev-neuro-100120-122621.

[112] R. Kottmeier *et al.*, "Wrapping glia regulates neuronal signaling speed and precision in the peripheral nervous system of Drosophila," *Nat. Commun.*, vol. 11, no. 1, Art. no. 1, Sep. 2020, doi: 10.1038/s41467-020-18291-1.

[113] M. E. Madden *et al.*, "CNS Hypomyelination Disrupts Axonal Conduction and Behavior in Larval Zebrafish," *J. Neurosci. Off. J. Soc. Neurosci.*, vol. 41, no. 44, pp. 9099–9111, Nov. 2021, doi: 10.1523/JNEUROSCI.0842-21.2021.

[114] B. P. Heithoff, K. K. George, A. N. Phares, I. A. Zuidhoek, C. Munoz-Ballester, and S. Robel, "Astrocytes are necessary for blood–brain barrier maintenance in the adult mouse brain," *Glia*, vol. 69, no. 2, pp. 436–472, 2021, doi: 10.1002/glia.23908.

[115] R. J. Bainton, L. T.-Y. Tsai, T. Schwabe, M. DeSalvo, U. Gaul, and U. Heberlein, "moody encodes two GPCRs that regulate cocaine behaviors and blood-brain barrier permeability in Drosophila," *Cell*, vol. 123, no. 1, pp. 145–156, Oct. 2005, doi: 10.1016/j.cell.2005.07.029.

[116] T. Schwabe, R. J. Bainton, R. D. Fetter, U. Heberlein, and U. Gaul, "GPCR Signaling Is Required for Blood-Brain Barrier Formation in Drosophila," *Cell*, vol. 123, no. 1, pp. 133–144, Oct. 2005, doi: 10.1016/j.cell.2005.08.037.

[117] T. Stork, D. Engelen, A. Krudewig, M. Silies, R. J. Bainton, and C. Klämbt, "Organization and Function of the Blood–Brain Barrier in Drosophila," *J. Neurosci.*, vol. 28, no. 3, pp. 587–597, Jan. 2008, doi: 10.1523/JNEUROSCI.4367-07.2008.

[118] Z. Ma, T. Stork, D. E. Bergles, and M. R. Freeman, "Neuromodulators signal through astrocytes to alter neural circuit activity and behaviour," *Nature*, vol. 539, no. 7629, Art. no. 7629, Nov. 2016, doi: 10.1038/nature20145.

[119] J. E. Melom and J. T. Littleton, "Mutation of a NCKX Eliminates Glial Microdomain Calcium Oscillations and Enhances Seizure Susceptibility," *J. Neurosci.*, vol. 33, no. 3, pp. 1169–1178, Jan. 2013, doi: 10.1523/JNEUROSCI.3920-12.2013.

[120] A. J. Gleichman and S. T. Carmichael, "Glia in neurodegeneration: Drivers of disease or along for the ride?," *Neurobiol. Dis.*, vol. 142, p. 104957, Aug. 2020, doi: 10.1016/j.nbd.2020.104957.

[121] E. Blanco-Suárez, A. L. M. Caldwell, and N. J. Allen, "Role of astrocyte-synapse interactions in CNS disorders," *J. Physiol.*, vol. 595, no. 6, pp. 1903–1916, Mar. 2017, doi: 10.1113/JP270988.

[122] M. W. Salter and B. Stevens, "Microglia emerge as central players in brain disease," *Nat. Med.*, vol. 23, no. 9, Art. no. 9, Sep. 2017, doi: 10.1038/nm.4397.

[123] D. C. Patel, B. P. Tewari, L. Chaunsali, and H. Sontheimer, "Neuron–glia interactions in the pathophysiology of epilepsy," *Nat. Rev. Neurosci.*, vol. 20, no. 5, Art. no. 5, May 2019, doi: 10.1038/s41583-019-0126-4.

[124] T. Stork, A. Sheehan, O. E. Tasdemir-Yilmaz, and M. R. Freeman, "Neuron-Glia Interactions through the Heartless FGF Receptor Signaling Pathway Mediate Morphogenesis of Drosophila Astrocytes," *Neuron*, vol. 83, no. 2, pp. 388–403, Jul. 2014, doi: 10.1016/j.neuron.2014.06.026.

[125] E. G. Hughes, S. H. Kang, M. Fukaya, and D. E. Bergles, "Oligodendrocyte progenitors balance growth with self-repulsion to achieve homeostasis in the adult brain," *Nat. Neurosci.*, vol. 16, no. 6, Art. no. 6, Jun. 2013, doi: 10.1038/nn.3390.

[126] J. Wang, M. L. O'Sullivan, D. Mukherjee, V. M. Puñal, S. Farsiu, and J. N. Kay, "Anatomy and spatial organization of Müller glia in mouse retina," *J. Comp. Neurol.*, vol. 525, no. 8, pp. 1759–1777, 2017, doi: 10.1002/cne.24153.

[127] M. C. Kremer, C. Jung, S. Batelli, G. M. Rubin, and U. Gaul, "The glia of the adult Drosophila nervous system," *Glia*, vol. 65, no. 4, pp. 606–638, 2017, doi: 10.1002/glia.23115.

[128] V. Hartenstein, "Morphological diversity and development of glia in Drosophila," *Glia*, vol. 59, no. 9, pp. 1237–1252, 2011, doi: 10.1002/glia.21162.

[129] N. Pogodalla, H. Kranenburg, S. Rey, S. Rodrigues, A. Cardona, and C. Klämbt, "Drosophila ßHeavy-Spectrin is required in polarized ensheathing glia that form a diffusion-barrier around the neuropil," *Nat. Commun.*, vol. 12, no. 1, Art. no. 1, Nov. 2021, doi: 10.1038/s41467-021-26462-x.

[130] J. Doherty, M. A. Logan, O. E. Taşdemir, and M. R. Freeman, "Ensheathing glia function as phagocytes in the adult Drosophila brain," *J. Neurosci. Off. J. Soc. Neurosci.*, vol. 29, no. 15, pp. 4768–4781, Apr. 2009, doi: 10.1523/JNEUROSCI.5951-08.2009.

[131] T. Lee and L. Luo, "Mosaic Analysis with a Repressible Cell Marker for Studies of Gene Function in Neuronal Morphogenesis," *Neuron*, vol. 22, no. 3, pp. 451–461, Mar. 1999, doi: 10.1016/S0896-6273(00)80701-1.

[132] S.-L. Lai and T. Lee, "Genetic mosaic with dual binary transcriptional systems in Drosophila," *Nat. Neurosci.*, vol. 9, no. 5, Art. no. 5, May 2006, doi: 10.1038/nn1681.

[133] J. Schindelin *et al.*, "Fiji: an open-source platform for biological-image analysis," *Nat. Methods*, vol. 9, no. 7, Art. no. 7, Jul. 2012, doi: 10.1038/nmeth.2019.

[134] D. Malin, "Unsharp Masking," *Am. Astron. Soc. Photo-Bull.*, vol. 16, pp. 10–13, 1977.

[135] N. Otsu, "A Threshold Selection Method from Gray-Level Histograms," *IEEE Trans. Syst. Man Cybern.*, vol. 9, no. 1, pp. 62–66, Jan. 1979, doi: 10.1109/TSMC.1979.4310076.

[136] G. W. Zack, W. E. Rogers, and S. A. Latt, "Automatic measurement of sister chromatid exchange frequency.," *J. Histochem. Cytochem.*, vol. 25, no. 7, pp. 741–753, Jul. 1977, doi: 10.1177/25.7.70454.

[137] C. H. Li and P. K. S. Tam, "An iterative algorithm for minimum cross entropy thresholding," *Pattern Recognit. Lett.*, vol. 19, no. 8, pp. 771–776, Jun. 1998, doi: 10.1016/S0167-8655(98)00057-9.

[138] C. H. Li and C. K. Lee, "Minimum cross entropy thresholding," *Pattern Recognit.*, vol. 26, no. 4, pp. 617–625, Apr. 1993, doi: 10.1016/0031-3203(93)90115-D.

[139] J.-C. Yen, F.-J. Chang, and S. Chang, "A new criterion for automatic multilevel thresholding," *IEEE Trans. Image Process.*, vol. 4, no. 3, pp. 370–378, Mar. 1995, doi: 10.1109/83.366472.

[140] R. M. Haralick, S. R. Sternberg, and X. Zhuang, "Image Analysis Using Mathematical Morphology," *IEEE Trans. Pattern Anal. Mach. Intell.*, vol. PAMI-9, no. 4, pp. 532–550, Jul. 1987, doi: 10.1109/TPAMI.1987.4767941.

[141] J. Shi, H. Zhang, and N. Ray, "Solidity based local threshold for oil sand image segmentation," in *2009 16th IEEE International Conference on Image Processing (ICIP)*, Nov. 2009, pp. 2385–2388. doi: 10.1109/ICIP.2009.5414517.

[142] M. Liukkonen, H. Mutikainen, J. Käyhkö, K. Peltonen, and H. Yrjö, "Approach for Online Characterization of Bubbles in Liquid by Image Analysis: Application to Oxygen Delignification Process," *Int. J. Comput. Inf. Syst. Ind. Manag. Appl.*, vol. 7, pp. 181–188, Nov. 2015.

[143] E. L. Nichols, L. A. Green, and C. J. Smith, "Ensheathing cells utilize dynamic tiling of neuronal somas in development and injury as early as neuronal differentiation," *Neural Develop.*, vol. 13, no. 1, p. 19, Aug. 2018, doi: 10.1186/s13064-018-0115-8.

[144] R. Srinivasan *et al.*, "New Transgenic Mouse Lines for Selectively Targeting Astrocytes and Studying Calcium Signals in Astrocyte Processes In Situ and In Vivo," *Neuron*, vol. 92, no. 6, pp. 1181–1195, Dec. 2016, doi: 10.1016/j.neuron.2016.11.030.

[145] M. M. Halassa, T. Fellin, H. Takano, J.-H. Dong, and P. G. Haydon, "Synaptic Islands Defined by the Territory of a Single Astrocyte," *J. Neurosci.*, vol. 27, no. 24, pp. 6473–6477, Jun. 2007, doi: 10.1523/JNEUROSCI.1419-07.2007.

[146] J. Degen *et al.*, "Dual reporter approaches for identification of Cre efficacy and astrocyte heterogeneity," *FASEB J.*, vol. 26, no. 11, pp. 4576–4583, 2012, doi: 10.1096/fj.12-207183.

[147] E. Z. Macosko *et al.*, "Highly Parallel Genome-wide Expression Profiling of Individual Cells Using Nanoliter Droplets," *Cell*, vol. 161, no. 5, pp. 1202–1214, May 2015, doi: 10.1016/j.cell.2015.05.002.

[148] A. M. Klein *et al.*, "Droplet Barcoding for Single-Cell Transcriptomics Applied to Embryonic Stem Cells," *Cell*, vol. 161, no. 5, pp. 1187–1201, May 2015, doi: 10.1016/j.cell.2015.04.044.

[149] P. Hasel, I. V. L. Rose, J. S. Sadick, R. D. Kim, and S. A. Liddelow, "Neuroinflammatory astrocyte subtypes in the mouse brain," *Nat. Neurosci.*, vol. 24, no. 10, Art. no. 10, Oct. 2021, doi: 10.1038/s41593-021-00905-6.

[150] B. S. Khakh and B. Deneen, "The Emerging Nature of Astrocyte Diversity," *Annu. Rev. Neurosci.*, vol. 42, no. 1, pp. 187–207, 2019, doi: 10.1146/annurev-neuro-070918-050443.

[151] Q. Li *et al.*, "Developmental Heterogeneity of Microglia and Brain Myeloid Cells Revealed by Deep Single-Cell RNA Sequencing," *Neuron*, vol. 101, no. 2, pp. 207-223.e10, Jan. 2019, doi: 10.1016/j.neuron.2018.12.006.

[152] V. Kis, B. Barti, M. Lippai, and M. Sass, "Specialized Cortex Glial Cells Accumulate Lipid Droplets in Drosophila melanogaster," *PLOS ONE*, vol. 10, no. 7, p. e0131250, Jul. 2015, doi: 10.1371/journal.pone.0131250.

[153] R. M. Beckervordersandforth, C. Rickert, B. Altenhein, and G. M. Technau, "Subtypes of glial cells in the Drosophila embryonic ventral nerve cord as related to lineage and gene expression," *Mech. Dev.*, vol. 125, no. 5–6, pp. 542–557, 2008, doi: 10.1016/j.mod.2007.12.004.

[154] R. M. Golovin, J. Vest, D. J. Vita, and K. Broadie, "Activity-Dependent Remodeling of Drosophila Olfactory Sensory Neuron Brain Innervation during an Early-Life Critical Period," *J. Neurosci.*, vol. 39, no. 16, pp. 2995–3012, Apr. 2019, doi: 10.1523/JNEUROSCI.2223-18.2019.

[155] A. S. Thum and B. Gerber, "Connectomics and function of a memory network: the mushroom body of larval Drosophila," *Curr. Opin. Neurobiol.*, vol. 54, pp. 146–154, Feb. 2019, doi: 10.1016/j.conb.2018.10.007.

[156] L. Venkatasubramanian and R. S. Mann, "The development and assembly of the Drosophila adult ventral nerve cord," *Curr. Opin. Neurobiol.*, vol. 56, pp. 135–143, Jun. 2019, doi: 10.1016/j.conb.2019.01.013.

Appendix

Code for Training CNN Globularity Classifier

For code used to conduct these analyses please see the following code repository:
https://github.com/gabys2006/GlobularityClassifier

Code Salazar et. al, 2022

For code used to conduct these analyses please see the following code repository:
https://github.com/gabys2006/TilingGlia

Sample Data

For a subset of the images that are part of the dataset analyzed in this thesis, please visit the Cell Image Library at UC San Diego cellimagelibrary.org/groups/54646